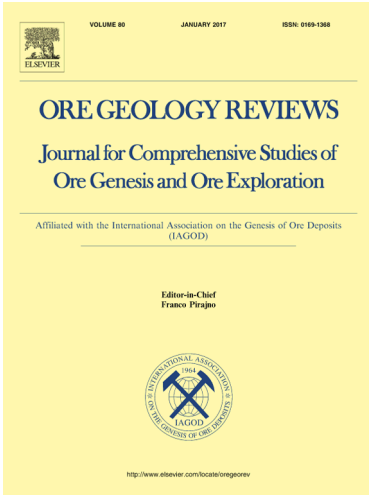

Mixing of magmatic-hydrothermal and metamorphic fluids and the origin of peribatholitic Sn vein-type deposits in Rwanda

J. Van Daele, N. Hulsbosch, S. Dewaele, M.-C. Boiron, K. Piessens, A. Boyce, Ph. Muchez

PII: S0169-1368(18)30323-8
DOI: https://doi.org/10.1016/j.oregeorev.2018.07.020
Reference: OREGEO 2637

To appear in: *Ore Geology Reviews*

Received Date: 18 April 2018
Revised Date: 5 July 2018
Accepted Date: 23 July 2018

Please cite this article as: J. Van Daele, N. Hulsbosch, S. Dewaele, M.-C. Boiron, K. Piessens, A. Boyce, Ph. Muchez, Mixing of magmatic-hydrothermal and metamorphic fluids and the origin of peribatholitic Sn vein-type deposits in Rwanda, *Ore Geology Reviews* (2018), doi: https://doi.org/10.1016/j.oregeorev.2018.07.020

Mixing of magmatic-hydrothermal and metamorphic fluids and the origin of peribatholitic Sn vein-type deposits in Rwanda.

Van Daele, J.[a*], Hulsbosch, N.[a], Dewaele, S.[b,c], Boiron, M.-C.[d], Piessens, K.[e], Boyce, A.[f] and Muchez, Ph.[a]

a KU Leuven, Geodynamics and Geofluids Research Group, Department of Earth and Environmental Sciences, Celestijnenlaan 200E, 3001 Leuven, Belgium

b Ghent University, Department of Geology, Krijgslaan 281, S8, 9000 Ghent, Belgium

c Royal Museum for Central Africa (RMCA), Department of Geology and Mineralogy, Leuvensesteenweg 13, 3080 Tervuren, Belgium

d Université de Lorraine, CNRS, GeoRessources, Boulevard des Aiguillettes B.P. 239, F-54000, Nancy, France

e Royal Belgian Institute of Natural Sciences, Geological Survey of Belgium, Jennerstraat 13, 1000 Brussels, Belgium

f Scottish Universities Environmental Research Centre, Rankine Avenue, East Kilbridge, Glasgow, G75 0QF, Scotland, U.K.

* corresponding author: johanna.vandaele@kuleuven.be

Keywords: leucogranite mineralization, pegmatites, cassiterite, quartz veins, fluid mixing, geochemical modelling

Abstract

The fluid sources of granite-related Sn-quartz vein deposits are commonly obscured by fluid mixing or fluid-rock interactions. As a result, fluid inclusions, minerals and isotopes in these veins indicate an intermediate composition between magmatic and metamorphic, but the degree of mixing between

these endmembers is currently unquantified. This study presents a novel quantitative approach to assess the degree of mixing between magmatic-hydrothermal and external metamorphic fluids in the formation of peribatholitic Sn-quartz veins. In particular, fluid mixing in the Sn-mineralized Rwamagana-Musha-Ntunga pegmatite-quartz vein field in East Rwanda has been evaluated by the following four methods: quartz stable isotopes, muscovite geochemistry, fluid inclusion microthermometry and LA-ICP-MS, and geochemical modelling.

The quartz stable isotope data ($\delta^{18}O$: +13.1 to +15.8 ‰ V-SMOW; δD: −27.6 to –59.7 ‰ V-SMOW) cannot uniquely differentiate between a metamorphic fluid origin or an initial magmatic hydrothermal fluid origin with subsequent metamorphic fluid mixing or host-rock interaction. However, granitophile element concentrations in magmatic muscovite from pegmatites and hydrothermal muscovite from associated Sn-quartz veins are equally high, indicating a close genetic link (Rb: 530 – 8740 ppm, Li: 110 – 1990 ppm, Sn: 87 – 810 ppm, Cs: 62 – 420 ppm). Primary H_2O-CO_2-N_2-NaCl medium saline magmatic fluid inclusions in quartz of pegmatites (~12.7 wt% $NaCl_{eq}$) and H_2O-CO_2-(N_2)-NaCl low saline fluid inclusions in barren metamorphic quartz veins (~4.9 wt% $NaCl_{eq}$) were analyzed by LA-ICP-MS. These results show an enrichment in Li, Rb, Sn and Cs for the magmatic fluid, while the metamorphic fluid is characterized by low granitophile element concentrations and high Sr and Ba contents. The expected Rb-Cs and Rb-Sn signature of the Sn-quartz vein muscovite was modelled using the measured fluid endmember compositions, confirming mixing between magmatic and metamorphic fluids in the formation of the veins. The quantification suggests that the hydrothermal Sn-quartz vein fluid contains 5 – 80 % of an external metamorphic fluid component.

1 Introduction

Tin and tungsten mineralization typically occurs in close proximity to differentiated leucogranites (figure 1). These deposits show a diversity of mineralization modes ranging from plutonic-hosted breccia and vein-stockwork systems to (peri-)batholitic greisens, skarns, pegmatites and hydrothermal veins (Baker et al., 2005). A direct genetic link between the mineralization and the

silicic magmatism is often debated, especially in the case of peribatholitic deposits (cf. Harlaux et al., 2017; Hulsbosch et al., 2016; Kozlik et al., 2016). Although a magmatic origin of the Sn or W mineralization is experimentally predicted (e.g. Heinrich, 1990; Pichavant and Manning, 1984; Wood and Samson, 2000), this signature is often obscured in nature by external fluid overprinting and quantifying the contribution of magmatic fluids as the principal metal-carrying phase is complex (Beuchat et al., 2004). Metamorphic or meteoric fluids can mix with and dilute fluids of magmatic origin or even potentially get enriched in metals by extraction from rocks within the circulation cell (Marignac and Cathelineau, 2010; Polya et al., 2000; Wilkinson, 1990). Audétat et al. (2000a), Williamson et al. (2010) and Hulsbosch et al. (2016) demonstrated, however, that granite-associated Sn and W mineralization were formed by magmatically-derived fluids, without any contribution from stripping of the country rocks by circulating hydrothermal fluids. Nevertheless, the signatures of fluid inclusions, minerals, bulk rock and isotopes in the mineralized quartz veins contradict the latter presumed magmatic origin (Hulsbosch et al., 2016). These findings were interpreted as the consequence of late-stage fluid-rock reactions or mixing with a metamorphic fluid (e.g. Chicharro et al., 2016; Dewaele et al., 2016a; Polya et al., 2000; Wilkinson, 1990). However, no effort has been made yet to quantitatively explain these masked signatures in detail.

Fig. 1 Schematic diagram illustrating primary granite-related W-Sn deposit styles in combination with their type-localities (1: North American Cordillera, 2: Bolivian province, 3: Iberian – Panasqueira province, 4: French Massif Central, 5: Cornwall, 6: Erzgebirge/Krušné Hory, 7: Kibara Metallogenic province, 8: southeast China province, 9: Myanmar-Thailand-Maleysia and 10: east Australian province). Styles partly after Baker et al. (2005). W-Sn province locations after Taylor (1979) and Beus (1986), Nb-Ta-Sn provinces after Melcher et al. (2016). Figure from Hulsbosch (2016).

The early-Neoproterozoic Nb-Ta-Sn-W metallogenetic province in the Karagwe-Ankole belt (KAB) of Central Africa provides a regional case study to evaluate the origin of peribatholitic Sn vein-type deposits and the degree of mixing of magmatic-hydrothermal and metamorphic fluids. The KAB

contains numerous granite-related ore deposits, in which the metals are present in lithium-cesium-tantalum (LCT) family pegmatites and associated greisens, as well as in Sn or W hydrothermal quartz veins. Tin-mineralized quartz veins are abundantly present in the Rwandese part of the KAB where they show a close temporal and spatial relationship to early-Neoproterozoic leucogranite and pegmatite intrusions (Brinckmann et al., 1994; Dewaele et al., 2016b; Tack et al., 2010). In particular, the abundant presence of cogenetic pegmatites and Sn-mineralized quartz veins around the Lake Muhazi leucogranite makes the Rwamagana-Musha-Ntunga area (RMN, East Rwanda) an ideal study area to constrain the genetic relation between the granite-pegmatite system and the Sn-mineralized quartz veins.

In this study we determined the primary magmatic fluid signature from fluid inclusions in pegmatitic quartz and the metamorphic fluid signature from metamorphic quartz. The term 'metamorphic fluid' is used in this article for fluids which have equilibrated with the metamorphic host rock and/or are the consequence of metamorphic dewatering processes. These fluid endmember data were used in combination with geochemistry of pegmatitic and quartz vein muscovite to constrain the contribution (i.e. degree of mixing) of metamorphic and magmatic fluids to the global fluid systems present around leucogranites during granite-pegmatite differentiation and the genesis of hydrothermal Sn quartz veins at the Rwamagana-Musha-Ntunga area (RMN).

2 Geology of the metallogenetic province in the KAB

2.1 Geological setting of the KAB

The Karagwe-Ankole belt (KAB) is a NE-SW trending belt located in Central Africa, covering parts of D.R. Congo, Rwanda, Burundi, Uganda and Tanzania. The KAB consists of Palaeo- and Mesoproterozoic supracrustal units, mostly metasedimentary rocks with minor metavolcanics (Fernandez-Alonso et al., 2012; Tack et al., 2010). In Rwanda (and the western part of Burundi and southwest Uganda), the Mesoproterozoic rocks of the KAB are assigned to the Akanyaru Supergroup, subdivided in four groups, from bottom to top the Gikoro, Pindura, Cyohoha and Rugezi Groups

(Baudet et al., 1988; Fernandez-Alonso et al., 2012). The Rwamagana-Musha-Ntunga area (figure 2) is part of the Western Domain of the KAB (Tack et al., 2010). The metasediments hosting the mineralized pegmatites and quartz veins belong to the Gikoro and Pindura Group (Hanon and Rusanganwa, 1991), deposited between 1420 Ma and 1375 Ma (Fernandez-Alonso et al., 2012).

A first generation of S-type granites, the G1-G3 granites in Rwanda, intruded the metasediments of the KAB at c.1375 Ma (Tack et al., 2010). In the early Neoproterozoic, a second generation of S-type granites, regionally termed the G4-granites, was emplaced (976 ± 10 Ma; Rb-Sr errorchron; Cahen and Ledent, 1979; 986 ± 10 Ma; SHRIMP U-Pb dating on zircons; Tack et al., 2010). Multiple granite-related Nb-Ta-Sn-W ore deposit types are temporally and spatially associated with the G4-granites in Rwanda. Tantalum-niobium-oxide and cassiterite mineralization can be present in granitic LCT-family pegmatites, aged between 975 and 963 Ma (Rb-Sr muscovite; Brinckmann and Lehmann, 1983; Monteyne-Poulaert et al., 1962; Rb-Sr whole rock; Lehmann et al., 1994; U-Pb columbite; Brinckmann et al., 2001; Dewaele et al., 2011; Melcher et al., 2015; Romer and Lehmann, 1995). Greisenization is reported in isolated zones ('pockets') in pegmatites, as an intense development of sericite crystals which recrystallized to larger muscovite sheets under influence of continuing K-alteration. Cassiterite mineralization in pegmatites is most often closely associated with these greisen pockets, which were dated at 904 ± 0.7 Ma (Dewaele et al., 2011; Varlamoff, 1972). Hydrothermal quartz veins can contain cassiterite (SnO_2) or W-bearing minerals (figure 2; Pohl, 1994; Tack et al., 2010). Ages of 992.4 ± 1.5 Ma and 984 ± 2.4 Ma have been obtained for the W-mineralized quartz veins (Ar-Ar muscovite; De Clercq, 2012; Dewaele et al., 2016a), while Sn-mineralized quartz veins have been dated at 965 ± 29 Ma (Rb-Sr muscovite; Monteyne-Poulaert et al., 1962) and 957 ± 21 Ma (U-Pb cassiterite; Zhang et al., 2016) . These two quartz vein types (W- and Sn-mineralized) do not show a close spatial relationship to each other (cfr. figure 2), because of the strong lithological host rock control. Sn-bearing quartz veins occur in muscovite-feldspar rich sandstone and quartzite, while organic-rich metapelites form the host rock of the W-mineralized quartz veins (De Clercq, 2012; Hulsbosch et al., 2016).

Fig. 2 Distribution of lithological groups, granite intrusions and Nb-Ta-Sn-W mineralization in Rwanda. 1 = Rwamagana city, 2 = Musha-Ntunga, 3 = Kigali city, 4 = Nyakabingo, 5 = Rutongo, 6 = Gatumba, 7 = Kibuye city. The Rwamagana-Musha-Ntunga study area is indicated with the blue rectangle. Modified after Fernandez-Alonso et al. (2007).

Around 1000 Ma, at the beginning of the Neoproterozoic, compressional events are reported in the KAB causing the morpho-structural shaping (Tack et al., 2010). The exact timing of metamorphism currently is not well-constrained and topic of research in progress. The lack of foliation and absence of metamorphic mineral growth in the G4-granites and pegmatites strongly suggest peak metamorphism in the KAB took place prior to their emplacement (i.e. 986 ± 10 Ma; Tack et al., 2010). However, ages of 962 ± 7 Ma (SHRIMP U-Pb garnet; de Kock et al., 2014) and 966 ± 11 Ma (SHRIMP U-Pb zircon overgrowths; Tack et al., 2010) have been interpreted to represent the peak of metamorphism, which is not in accordance with the clear petrographical evidence. These ages could be related to the G4-granite emplacement, such as contact metamorphic effects. . Regional metamorphism of the Mesoproterozoic sedimentary rocks of the KAB was generally low-grade greenschist facies (Baudet et al., 1988; Gérards and Ledent, 1970), but local excursions towards amphibolite facies have been reported in the vicinity of granite batholiths (Fernandez-Alonso et al., 2012; Tack et al., 1994).

Barren, metamorphic quartz veins in the KAB, as e.g. observed in the Kibuye and Gitarama areas (figure 2), typically occur as quartz pods in the hinges of folds or as folded bedding-parallel or bedding-perpendicular veins. Some of these quartz veins have a biotite-garnet rim (e.g. figure 4e). Folded bedding-parallel veins (e.g. at Nyakabingo, Central Rwanda) are according to De Clercq (2012) almost completely composed of quartz crystals. Inside many of these metamorphic veins, aligned fragments of the metapelitic host rock occur. These host rock inclusions are parallel to the vein wall and follow the curvature of the veins. Next to host rock inclusions, also fluid inclusion planes occur which crosscut the quartz crystals. The presence of the aligned host rock inclusions and the parallel

fluid inclusion planes points to a crack-seal mechanism for the formation of the veins (cf. Passchier and Trouw, 2005). The folded veins have been (sometimes intensely) fractured and coated by iron oxides. A small alteration zone can be observed at the contact zone between the folded veins and the host rock (De Clercq, 2012). Bedding-perpendicular metamorphic veins deflect the axial planar foliation present in the host rock, indicating their pre-foliation age (e.g. figure 4c-d).

2.2 The granite-pegmatite-quartz vein system in Rwanda and the Rwamagana-Musha-Ntunga area

In the Rwamagana-Musha-Ntunga area, the Lake Muhazi granite intrusion occurs in the center of the Karehe anticline (figure 3; Hanon and Rusanganwa, 1991). This anticline consists of metasediments of the Nyabugogo, Musha, Nduba and Bulimbi formations (a detailed lithological description can be consulted in Hulsbosch et al., 2017). The Bulimbi Formation belongs to the Pindura Group, while the other three formations to the older Gikoro Group (Hanon and Rusanganwa, 1991). Because of intense lateritization, only few fresh exposures of the granite are present (Varlamoff, 1969). Therefore, the outlines of the granite batholith have mainly been proposed based on the topographic morphology, i.e. a large depression without strong secondary relief (Hanon and Rusanganwa, 1991). Mineralization is present as Nb-Ta-Sn pegmatites and Sn-rich hydrothermal quartz veins (Hanon and Rusanganwa, 1991).

Fig. 3 Geological map of the Rwamagana-Musha-Ntunga area with indication of pegmatite and quartz vein occurrence (after Hanon and Rusanganwa, 1991; Hulsbosch et al., 2017).

The first detailed regional mapping of the pegmatite and Sn-quartz vein outcrops in the RMN area has been performed by Varlamoff (1969). This study identified six different mineralogical dyke and vein types around the Lake Muhazi leucogranite intrusion (Table 1). Due to intense albitization, greisenization and kaolinization of the Musha-Ntunga pegmatite system, no internal mineralogical zonation sequence can be observed within individual dykes. Based on reports by Varlamoff (1969) on historic mining activities, internally zoned Nb-Ta-Sn pegmatite dykes with quartz core development and amblygonite can be locally observed which transition towards strongly albitized Nb-Ta-Sn

pegmatite dykes with quartz, lepidolite and elbaite cores. Moreover, a transition from these LCT pegmatites to quartz-muscovite-cassiterite veins and partly albitized quartz-microcline-cassiterite-muscovite veins is observed at depth in the Ntunga mine in Rwanda (Hulsbosch et al., 2017; Varlamoff, 1969). The pegmatites of the mine sites of Musha and Ntunga belong dominantly to the type E of Varlamoff (1969) (Table 1). Pegmatites mainly occur as exogranitic in the RMN study area, although both endo- as exogranitic pegmatites are observed in Rwanda.

Table 1 Pegmatite and quartz vein mineralogy in the Rwamagana-Musha-Ntunga area (Varlamoff, 1969).

The pegmatites studied are intensely kaolinitized with some relicts of feldspar, and also contain various amounts of quartz and muscovite (figure 4a). Quartz occurs as randomly distributed, equigranular crystals or as grey to transparent quartz cores in the center of the pegmatites. These quartz megacrysts easily reach 6 cm * 6 cm * 6 cm in size. Muscovite (transparent white to green) can be present randomly dispersed throughout the pegmatite or concentrated around quartz or at the contact of the pegmatite with the host rock. The muscovite crystals can attain a size up to 5 cm * 5 cm * 1 cm. Columbite and tantalite (Coltan Group Minerals, CGM) and cassiterite mineralization is present as a disseminated phase in most of the pegmatites (Van Daele, 2016).

In the barren and Sn-bearing quartz veins, two main morphologies of quartz crystals are observed: pure transparent-white, blocky quartz and fine-crystalline, pale white saccharoidal quartz. Muscovite is often observed, in various positions in the quartz vein. It can be present in the center and at the edge of the vein (figure 4b), but also as pervasive muscovitization/sericitization of the host rock next to the quartz vein. Black tourmaline regularly occurs, mostly at the border of the quartz veins or disseminated in the host rock adjacent to the veins (Van Daele, 2016). The quartz veins are often mineralized in cassiterite (cf. type F of Varlamoff (1969); Table 1). Both pegmatites crosscut by quartz veins and quartz veins crosscut by small pegmatites were observed (figure 4b, Reinders, 2016). The

quartz veins in the Rwamagana-Musha-Ntunga area either follow the bedding (N20W-strike) or are EW oriented (Hulsbosch et al., 2017).

Due to the weathered character of the granite outcrops and the lack of a well-established regional and internal zoning in the RMN pegmatites, clear textural in-situ evidence for a genetic link between granites and pegmatites, as e.g. observed for the Tregonning Granite and pegmatite-aplite Megiliggar Sheet Complex in Cornwall (Breiter et al., 2018), cannot be determined in the Rwamagana-Musha-Ntunga granite-pegmatite system. Previous studies on the petro- and metallogenesis of the Rwandase LCT pegmatite systems and W-bearing quartz veins (Hulsbosch et al. 2014, 2016) applied mineral assemblages and mineral chemistry to allow the identification of Rayleigh fractional crystallization as the main process in the granite-pegmatite system (Gitarama-Gatumba area, West Rwanda; Hulsbosch et al., 2014). This differentiation process is reflected in a regional zoning from parental G4 leucogranites, biotite over 2-mica to muscovite and eventually Sn-Ta-Nb mineralized pegmatites. The most fractionated mineralized pegmatites associated with G4 parental granites were classified as the lithium-cesium-tantalum (LCT-) family, rare element class of Černý and Ercit (2005) (Dewaele et al., 2011). Furthermore, the link between W-mineralized quartz veins on the one hand and the granite-pegmatite system on the other hand was recently established. Fluid exsolution at the transition from granitic to pegmatitic melt was identified as the main process resulting in peribatholitic W-mineralized quartz veins in the Nyakabingo area, Central Rwanda (Hulsbosch et al., 2016). When the magmatic fluid exsolves from granitic or pegmatitic melt, elements with high fluid/melt partition coefficients preferentially partition in this exsolving fluid. It was observed that in granite-pegmatite systems, W shows a high affinity for an exsolving magmatic fluid phase, which can culminate in W-mineralized quartz veins (Hulsbosch et al., 2016).

Quartz veins in the KAB, either barren or mineralized, in spatial association with magmatic intrusions show a compositionally mixed metamorphic-magmatic fluid inclusion signature (e.g. Dewaele et al., 2016a; Hulsbosch et al., 2016). This is the case for fluid inclusions (FI) in quartz veins associated with

the W quartz vein-type deposits in Nyakabingo, Central Rwanda (12 quartz vein samples, 306 FI studied with microthermometry, 45 FI with LA-ICP-MS; De Clercq, 2012; De Clercq et al., 2008; Dewaele et al., 2016a). Fluid inclusions in quartz veins from the Sn-mineralized district of Rutongo, Central Rwanda, show similar characteristics (4 quartz vein samples, 164 FI; De Clercq, 2012; Dewaele et al., 2010). These mixed signatures have been attributed to overprinting of the pristine magmatic signature by metamorphic interaction at the deposit site, which can be related to the thermal activity of the regional granite intrusions in the area (cf. Prochaska et al., 1992). Consequently, fluid inclusions from barren, metamorphic quartz veins near granitic intrusions or pegmatite fields cannot be assumed to be representative as such for the pristine, metamorphic "background" fluid composition.

Fig. 4 Petrography of the pegmatites and quartz veins: a) pegmatite (mu = muscovite, qz = quartz, kaol kaolinite, fsp = feldspar), b) pegmatite crosscutting quartz vein with muscovite rim, c) folded metamorphic quartz vein perpendicular to the bedding, d) inset of c), quartz vein deflects host rock axial planar cleavage, e) bedding-parallel, metamorphic quartz vein with biotite-garnet rim, indicated in red.

3 Methodology

3.1 Samples and locations

Nine quartz separates of tin-bearing quartz vein samples from the RMN area are analyzed for their oxygen and hydrogen isotope composition. From different sample collections at the RMCA and the KU Leuven, Sn-mineralized and barren quartz vein samples are taken for a petrographic study of the fluid inclusions in double-polished wafers. This selection includes quartz from the Rwamagana-Musha-Ntunga, Kibuye and Gatumba areas (figure 2). Representative samples from the magmatic-hydrothermal and metamorphic fluids are selected for a detailed microthermometric and geochemical (LA-ICP-MS) fluid inclusion study.

Thirty-three samples of muscovite are selected from different mineralized and barren pegmatites and quartz veins for ICP-OES and ICP-MS analyses. Care was taken to only sample primary muscovite showing no signs of secondary alteration or weathering (based on color, luster and crystal morphology). In the case of pegmatitic muscovite, only coarse-grained, intergranular muscovite flakes which formed randomly in the dykes have been sampled. This texture indicates a primary magmatic origin for the muscovite. Secondary micas have been reported in similar Rwandese pegmatite systems (Gatumba area; Western Rwanda), but occur dominantly as massive, fine-grained and non-oriented violet-gray to lavender-coloured aggregates of lepidolite replacing primary K-feldspars in the core units of the pegmatites (Hulsbosch et al., 2013). Also metasomatic greisen muscovite can occur in these pegmatites but typically occurs as pockets in the dyke together with quartz (Varlamoff, 1969; Dewaele et al., 2011). Both types of secondary, replacive micas have not been sampled in this study. In case of the quartz veins, most muscovite was sampled close to the boundary with the host rock. The dataset comprises quartz veins and pegmatite from different host rock lithologies.

3.2 Quartz isotope analysis

Separates from the selected Sn-bearing quartz veins in the RMN area are prepared according to the procedure described by Dewaele et al. (2016a). The hand-picked quartz separates are analyzed for oxygen and hydrogen isotopes at the Scottish Universities Environmental Research Center (SUERC, Glasgow) using a laser fluorination procedure, involving total sample reaction with excess ClF_3 and a CO_2 laser at temperatures in excess of 1500 °C (Sharp, 1990). All fluorinations resulted in 100% release of O_2 from the silicate lattice. This O_2 is converted to CO_2 by reaction with hot graphite and analyzed by a VG SIRA II spectrometer. Results are reported in standard notation ($\delta^{18}O$) as per mil (‰) deviations from Vienna Standard Mean Ocean Water (V-SMOW). Error of reproducibility is typically around ±0.3 ‰ during analyses. Hydrogen analysis is done by in vacuo bulk heating. 1 g of the quartz separate was analyzed using the method of Donnelly et al. (2001) and a VG-Micromass

Optima mass spectrometer. Samples are heated to a maximum of 700°C to release the fluids from fluid inclusions (but not molecular hydroxides; Gleeson et al., 2008). Results are reported in standard notation (δD) as per mil (‰) deviations from Vienna Standard Mean Ocean Water (V-SMOW). Error of reproducibility is typically around ±5 ‰ during analyses.

3.3 Muscovite geochemistry

Pure mineral separates are prepared according to the procedure presented in Hulsbosch et al. (2014). During this preparation, oxidized, impure (inclusion-bearing) or altered muscovite grains were consequently discarded. The major and minor element compositions (Al, Fe, K, Mg, Mn, Na, Si, Ti, Zn, Ba, Rb, Sn, Sr) are analyzed with a Varian 720 ES Inductively-Coupled Plasma Optical Emission Spectrometer (ICP-OES, KU Leuven, Belgium) after dissolution following the lithium-metaborate flux procedure of Suhr and Ingamells (1966). Standards Reference Materials NBS-70a, BCS-269, MA-N, NIST-610 and GA are used for calibration. The mica samples are digested by four acids (HNO_3, $HClO_4$, HF and HCl) to analyze the trace element contents (Cs, Li, Nb, Ta, W) with an Agilent 7700x Inductively-Coupled Plasma Mass Spectrometer (ICP-MS, KU Leuven, Belgium).

Analytical precision is calculated based on three independently prepared solutions of one mica sample (replicates). Precision is better than 2.3 % Relative Standard Deviation (RSD) for the ICP-OES analyses and better than 7.6 % RSD for the ICP-MS analyses. Reference standards NBS-70a and G-2 indicate that the accuracy of the ICP-OES results is better than 6 % for most elements. Exceptions are Ba (minimum recovery of 73.9 %), Fe (minimum recovery of 88.1 %) and Mn (recovery of 110.5 %). The accuracy of the ICP-MS results is assessed based on standards G-2 and GA. For most elements, it is better than 12.5 %. Exceptions are Li (recovery of 68 – 94 %) and Cs (recovery of 95 – 116 %).

3.4 Fluid inclusions: petrography, microthermometry and Raman spectrometry

Microthermometry of the fluid inclusions present in the magmatic and metamorphic quartz samples is conducted on a Linkam MDS600 heating and freezing stage, mounted on an Olympus BX51

microscope (cf. Muchez et al., 1994). Accuracy of the measurements is within ±0.2 °C for temperatures between -56.6 °C and 31.1 °C, and within ±1.0 °C for temperatures above 31.1 °C. Calibration is done using synthetic fluid inclusions (Syn Flinc, USA) of the H_2O-CO_2, H_2O-NaCl, H_2O-KCl and H_2O systems. Additionally, the melting point of an indium standard is used as a calibration point (T_m = 156 °C). To avoid stretching, leakage and decrepitation of the fluid inclusions in the quartz due to enhanced internal pressures, the samples are first cooled. Final melting temperatures of ice and clathrate are obtained by sequential freezing (Haynes, 1985) or cycling (Goldstein and Reynolds, 1994). Two-dimensional volume percentage of the aqueous liquid solution in the fluid inclusions, directly after clathrate melting, has been measured with the Linksys Software of Linkam during microthermometry (precision of ±1 %).

Fluid salinities of the aqueous-gaseous fluid inclusions have been calculated with the computer package Clathrates of Bakker (1997). The salinity of fluid inclusions in which $T_{m,clath}$ occurs in the presence of an aqueous solution and two carbonic phases (both liquid and vapour) can be modelled using the Q2 program of the computer package Clathrates (Bakker, 1997; Bakker and Brown, 2003). In this case, the equation of state of Duan et al. (1996) is used.

Raman analyses were made at the Royal Belgian Institute for Natural Sciences (RBINS) in Brussels (Belgium) using a Senterra-Bruker laser Raman microspectrometer, which was mounted on an Olympus BX50 microscope. A 532-nm green Diode-Pumped Solid State laser (DPSS; type R200-532) was used as excitation source, operating at 20 mW. A detailed description of the measurement procedure has been given by Piessens and Muchez (2009).

3.5 Laser-Ablation Inductively-Coupled Plasma Mass Spectrometry

Individual fluid inclusions were ablated with a GeoLas excimer laser (ArF, 193 nm, Microlas, Göttingen, Germany) at 5 Hz laser frequency and the aerosols were analysed with an Agilent 7500c quadrupole ICP-MS, equipped with a collision–reaction cell at the GeoRessources Laboratory (Nancy, France). In order to reduce elemental fractionation, the ablated material was carried in helium gas

(0.5 l/min), which was mixed with argon via a cyclone mixer (volume of 9.5 cm^3) prior to entering the ICP torch. Due to the relatively small inclusion diameter (20-50 µm located 10-50 µm below sample surface), it took typically <10 s to extract the whole content of the fluid inclusions. Each analytical series was limited to a maximum of 10 isotopes (^{7}Li, ^{23}Na, ^{24}Mg, ^{29}Si, ^{39}K, ^{85}Rb, ^{88}Sr, ^{118}Sn, ^{133}Cs and ^{182}W) in order to optimise the limits of detection (LODs) and precision. Dwell times of 100 ms for Si, of 200 ms for Li, Na, Mg, K and Sr and of 500 ms for Rb, Sn, Cs and W were chosen. A detailed description of the specific instrumental setup and performance is given in Leisen et al. (2012).

Obtained intensity ratios to Na (the internal standard) were converted to concentration ratios by external calibration against NIST 610 and 612 standard reference glasses. All spectra have been processed using the SILLS software package of Guillong et al. (2008), with the charge-balanced $NaCl_{eq}$ concentration of the fluid, obtained by microthermometry. As the fluid inclusion salinities are homogeneous throughout each wafer, an average $NaCl_{eq}$ salinity has been calculated for both samples based on the overall population. Limits of detection for a given element have been calculated according to Longerich et al. (1996) and Pettke et al. (2012).

4 Results

4.1 Stable isotopes

The oxygen and hydrogen isotope composition of tin-bearing quartz veins in the RMN area is displayed in table 2. The $\delta^{18}O$ values of the quartz veins are relatively homogeneous (+13.1 to +15.8 ‰ V-SMOW), but the δD values vary significantly (−27.6 to –59.7 ‰ V-SMOW; table 2). Maximum burial temperatures in the Central-Rwandese KAB region have been interpreted to amount 400 °C (Frisch, 1971). In addition, Vertriest (2014) estimated the temperature of quartz vein formation around 320 °C. Therefore, 350 °C was used as an approximate temperature of quartz precipitation to calculate the $\delta^{18}O$ value of the ambient fluid (Matsuhisa et al., 1979).

$$1000 * \ln(\alpha_{\mathrm{quartz-water}}) = 3.34 * 106 / T^2 - 3.31 .$$

At a temperature of 350 °C, the $\delta^{18}O$-ratio of the fluid varies between 7.8 and 10.5 ‰ V-SMOW. In a $\delta^{18}O$ – δD diagram (Figure 5), the values for quartz plot in the field for metamorphic water, with one sample in the field of primary magmatic water.

Table 2 Stable isotope data of Sn-bearing quartz vein samples from the Rwamagana-Musha-Ntunga area. All values are in ‰ V-SMOW.

Fig. 5 $\delta^{18}O$ – δD plot of the calculated and analyzed isotopic composition of the fluids present in the Sn-bearing quartz veins in the Rwamagana-Musha-Ntunga area. The global meteoric water line and the ranges of metamorphic water, magmatic water and water that interacted with organic matter are indicated for comparison (cf. Hoefs, 2015; Sheppard, 1986).

4.2 Major element composition of muscovite

The major element composition of muscovite from pegmatites and muscovite from quartz veins in the RMN area is largely similar (table A.1 in appendix). Nevertheless, compared to quartz vein muscovite, pegmatitic muscovite generally contains higher amounts of Al (33.5 – 38 versus mostly 34 – 36.5 wt% Al_2O_3), K (8.8 – 10.5 vs 8.6 – 10.1 wt% K_2O) and Mn (0.02 – 0.15 versus 0.01 – 0.08 wt% MnO), but less Si (43.3 – 45.2 versus 44.5 – 46.4 wt% SiO_2), Mg (<0.01 – 0.37 versus 0.01 – 0.49 wt% MgO), Na (0.4 – 0.9 versus 0.5 – 1.2 wt% Na_2O), Fe (mostly 0.4 – 2.5 versus 0.4 – 3.1 wt% Fe_2O_3) and Ti (0.01 – 0.22 versus 0.02 – 0.6 wt% TiO_2). Some of these observations can be explained by tetrahedral $Si^{4+} \leftrightarrow Al^{3+}$ substitution coupled with octahedral $Fe^{2+}/Mg^{2+} \leftrightarrow Al^{3+}$ substitution, also known as the Tschermak substitution [$Al_2 \leftrightarrow Si + (Fe,Mg)$] (Viana et al., 2007).

Tischendorf et al. (1997) proposed a classification scheme for micas based on the cations present in the octahedral site, more specifically on the parameters Mg – Li (mgli) and Fe + Ti + Mn – Al(VI) (feal). These parameters were calculated for each sample using the structural formula spreadsheet of Tindle (2001). The classification scheme of Tischendorf et al. (1997) confirms all white mica samples belong to the muscovite group.

4.3 Trace element concentrations in muscovite

Pegmatitic muscovite and quartz vein muscovite contains similar amounts of Li (110 – 1990 ppm versus 120 – 1670 ppm), Sn (120 – 810 versus 87 – 750 ppm), Cs (67 – 420, except for an outlier of 1180 ppm, versus 62 – 410 ppm) and W (1 – 17 versus 2 – 10 ppm). The elements Nb, Rb, Ta and Zn are enriched in pegmatitic muscovite relative to quartz vein muscovite (respectively 49 – 250 versus 19 – 110 ppm Nb, 1460 – 8740 versus 530 – 3780 ppm Rb, 10 – 104 versus 2 – 60 ppm Ta and 62 – 890 versus 38 – 380 ppm Zn). Quartz vein muscovite shows the highest values for Sr (6 – 76 versus 8 – 45 ppm) and Ba (22 – 2430 versus 12 – 310 ppm) (table 3). The geochemical signature of muscovite is not correlated to its textural setting (i.e. internally dispersed or concentrated at the margins) nor to the nature of the host rock.

Table 3 Trace element concentrations of Rwamagana-Musha-Ntunga muscovite samples. All values are in ppm.

It has been proposed that trace element variation in muscovite reflects modifications of the melt composition (Alfonso et al., 2003; Hulsbosch et al., 2014). Accordingly, the evolution in magmatic differentiation can be derived from compositional muscovite data. By analogy with other studies (Hulsbosch et al., 2013, 2014; Roda-Robles et al., 1999; Viana et al., 2007), K/Rb was chosen as the reference parameter to characterize geochemical trends of pegmatites and quartz veins expressed by alkali, alkali earth and rare metal contents in muscovite (figure 6).

In a log-log plot, K/Rb is positively correlated to Ba and to a lesser extent to W mainly for pegmatitic muscovite (figures 6a and 6i). Cs and Ta are negatively correlated to K/Rb for both quartz vein and pegmatitic muscovite (figures 6b and 6h). The highest Cs- and Ta-concentrations are found in muscovite that was sampled from Nb-Ta-Sn mineralized pegmatites and quartz veins. The Rb versus K/Rb plot (figure 6e) shows that quartz vein muscovite in most cases has a lower Rb-content than pegmatitic muscovite. Furthermore, the samples plot in two largely distinct groups regarding the Sr-concentration (figure 6g). The Sr-content of pegmatitic muscovite shows a positive correlation with

Rb-content. Li, Nb and Sn are not correlated to K/Rb (figures 6c, 6d and 6f). However, the elements Sn, Cs and Ta correlate positively to each other, especially for the pegmatitic muscovite. In contrast, W shows a negative correlation with these elements. The elements Nb and Li are not correlated to the Sn-content.

Fig. 6 Trace element concentrations of muscovite samples of the Rwamagana-Musha-Ntunga area. A distinction between non-mineralized and mineralized pegmatites and quartz veins is given.

4.4 Fluid inclusions

The last decade multiple combined petrographic and fluid inclusion studies were performed on quartz veins and associated magmatic systems in the KAB (see review in Hulsbosch, 2018). In order to define the magmatic and metamorphic fluid-endmembers and to subsequently calculate the degree of mixing between these fluid end-members in the formation of the Sn-mineralised veins of Musha-Ntunga, a top-down approach has been applied to select the most suitable samples. Multiple samples were selected for petrographical description. Subsequently, the most suitable samples were studied by fluid inclusion thermometry. Based on these results, samples were selected to determine the trace element composition of the fluid by LA-ICP-MS.

The characterization of the magmatic fluid end-member present in the Lake Muhazi granite-pegmatite system was done by investigating primary quartz from Nb-Ta mineralized pegmatite. The hydrothermal fluid composition in the Sn-quartz veins can be determined from quartz vein samples in the Musha-Ntunga area (figure 3). Three Nb-Ta mineralized pegmatites and 8 Sn-mineralized quartz veins were studied in detail by petrography. Based on these results, representative fluid inclusions from pegmatitic quartz were selected for microthermometry (n = 63) and LA-ICP-MS analyses (n = 43) to characterize the magmatic fluid endmember. Petrography demonstrated that the fluid inclusions in the Sn-mineralized quartz vein samples had undergone decrepitation and therefore could not be used to obtain representative results and could not be included in this study.

The original metamorphic fluid signature generally is not preserved in metamorphic quartz veins near magmatic intrusions in the KAB (cfr. De Clercq, 2012; De Clercq et al., 2008; Dewaele et al., 2016a, 2010; Hulsbosch et al., 2016). Therefore, the regionally present metamorphic fluid is characterized by means of metamorphic quartz veins sampled outside of the Rwamagana-Musha-Ntunga area. Fluid inclusions of five metamorphic quartz veins from the Kibuye and Gitarama areas (figure 2) were petrographically investigated. This preliminary study allowed to make a representative selection of the most pristine, metamorphic fluid inclusions for microthermometry (n = 52) and LA-ICP-MS analyses (n = 41).

4.4.1 Fluid inclusion petrography

Pegmatitic quartz shows clustered fluid inclusions with dimensions between 30 and 100 µm (figure 7a). All fluid inclusions show a negative crystal shape and contain three phases: an aqueous fluid phase, a gaseous liquid phase and a vapour bubble (figure 7b). Fluid inclusions can co-occur in assemblage with melt inclusions, which indicates their primary character and representativeness for the fluid present during magmatic stages of crystallization (figure 7c). In the case of barren, metamorphic quartz (from the Kibuye and Gitarama areas), subhedral primary fluid inclusions with diameters between 18 and 45 µm occur in clusters (figure 7d). Multiple generations of secondary inclusion trails are also present, but were discarded. The inclusions studied consist of three phases: an aqueous fluid phase, a gaseous liquid phase and a vapour bubble (figure 7d).

Fig. 7 (A) and (B) fluid inclusions in magmatic quartz, (C) coarsely crystallized melt inclusion in magmatic quartz, (D) fluid inclusions in metamorphic quartz.

4.4.2 Microthermometry

Representative microthermometric data of inclusions in magmatic and metamorphic quartz are given in table 4 and 5 respectively (n = 52 and 63 respectively).

The variation between different fluid inclusions in magmatic quartz is limited (table 4). The fluid inclusions show a 2D-calculated V_{gas} of 58 – 71 %. The melting temperature of CO_2 varies from -59.5 °C to -57.7 °C. First melting occurred at a temperature between -26.1 °C and -20.2 °C and all ice was molten when a temperature of -8.7 °C to -6.4 °C was reached. Dissociation of clathrate was observed at temperatures between 7.9 °C to 8.6 °C. The CO_2-homogenization (to liquid) temperature varies between 29.6 °C and 31.2 °C and the fluid inclusions were totally homogenized at 299 – 312 °C. Based on Raman analysis an average gas composition of 80 mol% CO_2, 18 mol% N_2 and 2 mol% CH_4 could be determined for these fluid inclusions. The magmatic fluid inclusions are characterized as H_2O-CO_2-N_2-NaCl type fluid inclusions with an average amount of NaCl around 12.7 wt%.

Table 4 Microthermometric data of the H_2O-CO_2-N_2-NaCl fluid inclusions in magmatic quartz.

The primary fluid inclusions present in metamorphic quartz show minor variability (table 5). The V_{gas} is between 51 % and 60 %. The melting temperature of CO_2 varies from -57.5 °C to -56.5 °C. The temperature of first melting of ice could only be determined for a few fluid inclusions, at around -30 °C, but all ice was molten when a temperature of -4.1 °C to -2.4 °C was reached. Melting of the clathrate occurred at a temperature of 8.2 °C to 9.5 °C. CO_2-homogenization temperature (to liquid) was between 27.1°C and 30.7 °C. The total homogenization temperature could not be determined because of decrepitation. Raman analysis of these fluid inclusions indicates that the dominant gas (> 95 mol%) is CO_2 with traces of N_2 up to 5 mol% classifying these inclusions as of the H_2O-CO_2-(N_2)-NaCl-type. Salinity varies slightly between 3.9 and 5.9 wt% $NaCl_{eq}$, with an average of 4.3 wt% $NaCl_{eq}$, significantly lower than the NaCl-content of the fluid inclusions in magmatic quartz.

Table 5 Microthermometric data of the H_2O-CO_2-(N_2)-NaCl fluid inclusions in metamorphic quartz.

4.4.3 Fluid composition

In total, 84 inclusions were analyzed by LA-ICP-MS (tables 6 and 7, figure 8). Two ablation spectra are shown in figure 9. Forty-three inclusions were measured in magmatic quartz from the RMN area

(table 6). These show particular high contents of K (1.05 – 9.40 wt%) , Li (71 – 89300 ppm), Rb (9 – 5100 ppm), Sn (52 – 26400 ppm) and Cs (11 – 13900 ppm). W- and Sr-contents are relatively low (respectively <1 – 128 ppm and 5 – 520 ppm). In metamorphic quartz from the Kibuye area, 41 inclusions were successfully analyzed (table 7). These fluid inclusions are characterized by lower contents of Li (< 1420 ppm), Rb (< 120 ppm), Sn (<2 – 6220 ppm) and Cs (< 87 ppm). K and Na are the dominant cations but are present in lower amounts compared to the fluid present in magmatic quartz (0.03 – 5.36 wt% K and average 1.69 wt% Na). Sr- and W-concentrations are equally low compared to the magmatic fluid inclusions (2 – 2980 ppm and < 89 ppm respectively).

Table 6 Fluid inclusion LA-ICP-MS data of magmatic quartz from the RMN area. Values below limit of detection are displayed as <"DL".

Table 7 Fluid inclusion LA-ICP-MS data of metamorphic quartz from the Kibuye area. Values below limit of detection are displayed as <"DL".

Fig. 8 Fluid inclusion LA-ICP-MS data of magmatic and metamorphic quartz, from the RMN and Kibuye area, respectively. Samples with one of the parameters below the detection limit were given an arbitrary value of 1 ppm for that element to display them in the log-log diagrams.

Fig. 9 LA-ICP-MS spectra of two fluid inclusions in magmatic and metamorphic quartz, from the RMN and Kibuye area, respectively.

5 Interpretation and discussion

5.1 Quartz vein stable isotopes

Variable, low δD values combined with a narrow range of $\delta^{18}O$ values have been observed in several quartz vein-hosted Sn or W ore deposits (Dewaele et al., 2016a; Kelly and Rye, 1979; Patterson et al., 1981; Polya et al., 2000). Heinrich (1990) states that stable isotope data from nearly all Sn-W deposits indicate that the mineralizing fluids were equilibrated isotopically with a hot (> 400 °C) granitic source rock, prior to their transport into a cooler (< 400 °C) ore deposition site.

The differentiation between magmatic and metamorphic fluids in terms of $\delta^{18}O$ and δD is limited, making interpretations concerning the mixing of these two fluid phases difficult. Isotope analysis of quartz samples from the RMN Sn-mineralized veins indicates that the vein-forming fluids were indeed largely influenced by metamorphic processes or a metamorphic host rock – equilibrated fluid and, therefore, do not indicate a direct magmatic origin. The quartz stable isotope data furthermore justifies the assumption that meteoric fluids did not play a major role in the genesis of the RMN Sn-bearing quartz veins (see also Dewaele et al., 2016a, 2010). This is in agreement with the granite intrusion depth, which have been determined to be 10 – 16 km (Lehmann et al., 2014).

5.2 Fractional crystallization in the pegmatites

K/Rb versus Cs in muscovite has been reported to be a reliable indicator of pegmatite evolution (e.g. Černý et al., 1985; Jolliff et al., 1992; Oyarzábal et al., 2009; Roda-Robles et al., 2012; Vieira et al., 2011). During fractional crystallization, bulk incompatible elements get enriched in the residual melt, while bulk compatible elements get depleted. Trace element concentrations in the evolving melt (and precipitating crystals) obey the Rayleigh law of fractionation (Neumann et al., 1954). The concentration of a particular element in a mineral is dependent on its crystal-melt partition coefficient (K_d) and the melt concentration at the moment of precipitation. An evolutionary sequence throughout the crystallizing melt, as function of the crystallized fraction *F,* can be established quantitatively if the initial composition of the granitic melt, the mineral proportions during evolution and the required K_d values are known (cf. Hulsbosch et al., 2014; Jolliff et al., 1992; Roda-Robles et al., 1999). Rb and Cs are both bulk incompatible elements ($D > 1$) in granite-pegmatite systems (Martins et al., 2012; Saleh et al., 2008; Viana et al., 2007). Therefore, it is expected that the concentrations of these trace elements increase during fractional crystallization in the residual melt, which is consequently reflected in the muscovite geochemistry. Indeed, a negative trend in the Cs – K/Rb graph is observed (figure 6b), which is compatible with a progressive magmatic evolution by fractional crystallization. Furthermore, it was observed that Ba in pegmatitic muscovite shows a

positive correlation with the K/Rb-ratio (figures 6a). Crystallization of feldspars and micas has been reported to result in progressive depletion of Ba and Sr (Jolliff et al., 1992; Oyarzábal et al., 2009; Roda-Robles et al., 2012; Vieira et al., 2011).The Ba- data are thus likewise in accordance with an evolution that can be attributed to fractional crystallization. This is not the case for Sr, as a positive Rb-Sr correlation can be observed in figure 6g. Sr-content in muscovite increases from 10 to 30 ppm with increasing Rb (1000 – 10.000 ppm). The radioactive decay of ^{87}Rb to ^{87}Sr could be the cause of the positive correlation. This process has been reported to be significant for old, Rb-rich minerals (Černý et al., 2012), as is the case for the pegmatitic muscovite of the RMN area. Furthermore, significant Sr-loss due to post-crystallization mobility in pegmatite systems has been documented (Clark and Černý, 1987). Therefore, even though Sr generally behaves as a bulk incompatible element in a granite-pegmatite system due to the crystallization of feldspar, a negative Rb-Sr correlation is not always present and Sr-concentrations should not be used for geochemical interpretations (Černý et al., 2012; Clark and Černý, 1987). Sn-content was observed to be highest in muscovite from mineralized pegmatites. As stated by Smeds (1992), Sn-content of muscovite is a good indicator for the presence of cassiterite mineralization. Although the latter established the distinction between non-mineralized and mineralized pegmatites at 600 ppm Sn in muscovite, in the Rwamagana-Musha-Ntunga area this boundary is at about 400 ppm Sn (figure 6f).

It was not possible to obtain compositional data on the Lake Muhazi granite as no fresh outcrops of granite were observed in the Rwamagana-Musha-Ntunga area. This implies that the exact degree of fractional crystallization cannot be assessed directly. Therefore, muscovite data of this study is compared to the data and model for the Gitarama-Gatumba pegmatite field in West Rwanda (figure 2; Hulsbosch et al., 2014), which has a similar age, geological setting and petrological history. Based on muscovite and feldspar geochemistry, the regional mineralogical zonation of the pegmatites around the G4 Gitarama pluton could be quantified in terms of a petrogenetic sequence of Rayleigh fractional crystallization. This model shows an evolution of barren biotite-dominant (F = 0 – 0.69), over barren two-mica-dominant (F = 0.69 – 0.92) and barren muscovite-dominant (F = 0.92

– 0.98) common pegmatites to eventually Nb-Ta-Sn mineralized (*F* > 0.98) rare-element pegmatites (Hulsbosch et al., 2014). In terms of K/Rb-ratio and trace elements, the composition of pegmatitic muscovite from the RMN study area is in general very similar to that of muscovite from the muscovite- and mineralized-type pegmatites of the Gitarama-Gatumba (West-Rwanda; Hulsbosch et al., 2014, 2013), except for a relative enrichment in Sr for the RMN muscovites (10 – 30 ppm versus 1 – 6 ppm). A detailed comparison in terms of K, Rb and Cs content is given in figure 10. The Rb-content of the RMN pegmatite samples corresponds to that of Gitarama-Gatumba muscovite from pegmatites representing a fractionation degree of the parental granitic melt exceeding 0.92, i.e. from the muscovite and mineralized pegmatites (Hulsbosch et al., 2014). The RMN pegmatitic muscovite is relatively enriched in Cs compared to Gitarama-Gatumba muscovite: the samples correspond to a degree of fractionation higher than 0.98 regarding Cs-content.

Fig. 10 Comparison of Rwamagana-Musha-Ntunga muscovite samples of this study with the pegmatitic muscovite zonation model of Gitarama-Gatumba of Hulsbosch et al. (2014) and the Nyakabingo quartz vein muscovite samples of Hulsbosch et al. (2016). *F* represents the fraction of the melt that crystallized.

5.3 Furthermore, pegmatitic muscovite from the RMN area shows a slightly more fractionated signature compared to the LCT-family Sebago 'simple' pegmatites (southern Maine, USA; Wise and Brown, 2010) and the lower boundary zone pegmatites of the Pinilla de Fermoselle pegmatite system (Spain; Roda-Robles et al., 2012). This is expressed by a relative enrichment of Cs, Rb, Sr and Sn in the RMN pegmatitic muscovite. Other trace elements, such as Ba, Li, Nb and Ta are largely present in similar concentrations for the RMN and Sebago pegmatites, while the Pinilla de Fermoselle pegmatitic muscovite has lower Ba and Ta, and higher W and Li contents compared to the RMN muscovite (Roda-Robles et al., 2012). In contrast, the LCT Tanco pegmatite (Manitoba, Canada) is more fractionated than the RMN pegmatites. Compared to the muscovites analyzed in this study, the Tanco muscovite crystals show a lower K/Rb-ratio and higher Cs, Li, Rb

and Ta content (Van Lichtervelde et al., 2008). Nb-concentrations are lower, which possibly can be attributed to earlier crystallization of columbite ([Fe, Mn]Nb_2O_6). **Fluid mixing in the quartz veins**

5.3.1 Quartz vein muscovite

To determine if a magmatic (granitic or pegmatitic) component contributed to the fluid from which the Sn-mineralized quartz veins precipitated, the geochemical signature of quartz vein muscovite is compared to thatof pegmatitic muscovite. Quartz vein muscovite contains high amounts of Cs, similar to pegmatitic muscovite (figure 6b). A high Cs-content is not characteristic of a metamorphic fluid (cf. Marsala et al., 2013; Rauchenstein-Martinek et al., 2016), but rather indicates that the quartz veins precipitated from a fluid phase with a magmatic origin or component. K_{fm}-values (fluid-melt partition coefficient) of 0.4 to 8.6 (2.9 ± 2.6; n = 12) have been measured for Cs (Zajacz et al., 2008). A K_{fm} higher than unity indicates that Cs will preferentially partition in a fluid phase when present. Given the high affinity of Cs for an exsolving fluid, two possible hypotheses can explain the similar range of Cs-content observed in the quartz vein and pegmatitic muscovite samples. The first hypothesis postulates that the fluid exsolution took place from granitic or early pegmatitic melt which contains low amounts of Cs compared to the analyzed pegmatite muscovite samples. The second hypothesis is that the fluid exsolved from the pegmatites only in a late-stage, when these were already highly differentiated. Subsequently this fluid was diluted by a metamorphic fluid, especially concerning the granitophile, soluble elements, such as Cs.

In contrast to Cs, the Rb-content of quartz vein muscovite is considerably lower than that of pegmatitic muscovite (figure 6e). The K_{fm} values for Rb vary between 0.16 and 1.08 (0.5 ± 0.2; n = 12; Zajacz et al., 2008), indicating that Rb will be less partitioned from a melt into an exsolving fluid phase. A higher fluid compatibility for Cs compared to Rb has been reported by London (2005) and Dewaele et al. (2016b). This geochemical decoupling between Cs and Rb upon fluid exsolution is reflected in the muscovite data, which is an additional indication for a magmatic component in the

quartz vein fluid. Furthermore, trace elements Ba and Sr can display highly soluble K_{fm} values (Zajacz et al., 2008) and the data of this study show that quartz vein muscovite is enriched in Ba and Sr compared to pegmatitic muscovite. Accordingly the signatures of these alkali earth elements in muscovite are also in accordance with the hypothesis that the quartz veins at least partly originated from a magmatic fluid that exsolved from granitic or pegmatitic melt.

The large difference in Sr-content between pegmatitic and quartz vein muscovite can have multiple causes. One possibility is the crystallization of feldspar, in which Sr can substitute for Ca. Feldspars form a dominant constituent of the pegmatites (now kaolinitized), which could explain the relative depletion in Sr observed for this muscovite type. Alternatively the high K_{fm} of Sr and mixing with a metamorphic, Sr-rich fluid can be responsible for the relatively Sr-enriched character of quartz vein muscovite.

Muscovite from Sn-mineralized quartz veins in the RMN area contains 500 – 750 ppm Sn, which is high in comparison to other hydrothermal quartz vein systems mineralized in Sn, such as the W-Sn Panasqueira deposit, Portugal (226 ppm Sn; Neiva, 1987) and the hydrothermal W-Sn veins in Maoping, China (377 ± 4.5 ppm Sn; Legros et al., 2016). Despite this high Sn-content, no cassiterite inclusions were observed microscopically in muscovite. The positive correlation between Sn and Cs observed in hydrothermal muscovite from the Panasqueira, Montezinho, Argozelo and Borralha deposits in Portugal (Neiva, 1987) is also present in this dataset.

5.3.2 Fluid geochemistry

Based on the fluid inclusion geochemical signature, we propose that the medium saline fluid present in pegmatite-associated quartz from the Rwamagana-Musha-Ntunga area represents a magmatic fluid, exsolved upon water saturation of the pegmatitic melt. This fluid is particularly enriched in the bulk incompatible elements Rb, Cs and Sn. By fractional crystallization, bulk incompatible elements such as Rb, Cs and Sn progressively get enriched in the residual melt compared to the initial granitic melt. The melt from which fluid exsolves at a late stage is thus relatively enriched in these elements

compared to the melt from which an early-stage fluid would exsolve. This pre-concentration automatically is reflected in the composition of the exsolved fluid.. Additionally, Cs has a high fluid-melt partition coefficient (Zajacz et al., 2008). The presence of small cassiterite crystals can explain the highest Sn-contents occurring in some of the inclusions. These are observed as small black spots in the fluid inclusions (figure 7a). The magmatic fluid inclusions also show a slight relative depletion in Sr (compared to the metamorphic fluid), which is attributed to feldspar crystallization in the pegmatites, as the exsolution origin of this fluid would be expected to result in Sr-rich fluids (cf. the high K_{fm} for Sr; Zajacz et al., 2008). The low values of tungsten are in accordance with the model proposed by Hulsbosch et al. (2016) in which fluid exsolution at the granite-pegmatite transition scavenges the highly fluid-compatible W from the magmatic system and can give rise to early W-mineralized quartz veins (e.g. in Nyakabingo; Hulsbosch et al., 2016). The high Li-content can be due to small mineral inclusions such as zabuyelite (Li_2CO_3) or Li-mica inclusions.

The low-salinity fluid inclusions from metamorphic quartz (Kibuye area) represent the regionally present metamorphic fluid. This metamorphic fluid typically contains low amounts of Rb and Cs, often below the detection limit, but is slightly enriched in Sr compared to the primary magmatic fluid. The Rb-, Sn- and Cs-content of the fluid inclusions in this metamorphic quartz vein corresponds with the ranges observed in other metamorphic fluids (e.g. Fyfe et al., 1978 (7 ppm Sn); Marsala et al., 2013 (< 13 ppm Rb, < 74 ppm Cs); Rauchenstein-Martinek et al., 2016 (< 136 ppm Rb, < 35 ppm Cs)).

5.3.3 Geochemical mixing model

The exsolution of a fluid phase at the transition from G4-granite to pegmatite, i.e. prior to or early during pegmatite emplacement, has been inferred to give rise to W-mineralized hydrothermal quartz veins in the Nyakabingo area (Central Rwanda; figure 2), based on muscovite and fluid inclusion geochemistry, dating and modelling (Hulsbosch et al., 2016). When the samples of this study are compared to those of Hulsbosch et al. (2016) (figure 10), it can be observed that the Rwamagana-

Musha-Ntunga area quartz vein muscovite samples, both from barren and Sn-mineralized veins, have a K/Rb-ratio which is equal or lower than that of Nyakabingo quartz vein muscovite (cf. Hulsbosch et al., 2016), i.e. a higher Rb-content. The Cs-concentrations in muscovite samples of this study are very high compared to those of Nyakabingo quartz vein muscovite.

Based on the elevated Rb- and Cs-contents, an early exsolution event at the granite-pegmatite transition can be excluded, as illustrated in figure 11. This figure conceptually shows the change in geochemical signatures during exsolution, mixing and muscovite crystallization. No quantitative values were assigned, as this differs for each system. For the RMN Sn-quartz veins, the exsolution most likely occurred at a later stage, from a highly differentiated melt. Additionally, this corresponds to the field observations of cross-cutting relationships, which indicate that pegmatites and quartz veins were largely syngenetic (Hulsbosch et al., 2017). In this scenario, mixing with a metamorphic fluid is postulated to explain the observed Rb-Cs signature of quartz vein muscovite compared to pegmatitic muscovite (figure 11). This proposition is also consistent with the stable isotope data.

Fig. 11 Conceptual representation of (a) the expected muscovite signature, (b) the expected fluid signature and (c) the geological situation in case of early (1), intermediate (2) and late (3) exsolution and subsequent mixing.

Mixing of an exsolved magmatic fluid with a metamorphic fluid has already been inferred in other granite systems, e.g. the Cornubian batholith (England), based on bulk solute and volatile analyses of fluid inclusions (Wilkinson, 1990). Hydrothermal convection systems induced by granite intrusions have been indicated by thermodynamic modelling (e.g. Fehn, 1985), mineralogy, fluid inclusion and isotopic analyses (e.g. Boyce et al., 2003) and numerical modelling (e.g. Eldursi et al., 2009), i.e. metamorphic (host-rock equilibrated) fluids can be part of a hydrothermal convective system induced by a granite intrusion (Wilkinson, 1990).

The hypothesis of quartz vein genesis, i.e. a late exsolution event and mixing with a host rock fluid, can be quantitatively verified using the Rb-, Sn- and Cs-content of the magmatic and metamorphic

quartz vein fluids analyzed by LA-ICP-MS. The mixing trend between the initial magmatic fluid and the metamorphic fluid is calculated in order to simulate the composition of a mixed hydrothermal fluid. With the crystal/fluid partition coefficients for muscovite, the expected geochemical signature of muscovite precipitating from this calculated fluid can be determined. The comparison between the calculated and analyzed muscovite Rb-, Sn- and Cs-concentrations will test the pertinence of this petrogenetic hypothesis. Simultaneously, an estimation of the degree of mixing can be made.

The geochemical composition of the magmatic and metamorphic fluid endmembers that are used in the modelling, is summarized in table 8. The Rb-, Sn- and Cs-contents of the analyzed fluid inclusions for each endmember show a highly skewed distribution. Additionally, many values below the detection limit were measured for the fluid inclusions in the metamorphic quartz and some of the magmatic fluid inclusions contain very high amounts of Sn, which are attributed to the presence of small cassiterite inclusions. Therefore median values were used in further calculations. Values below the detection limit were substituted by the detection limit divided by $\sqrt{2}$, as proposed by Verbovsek (2011) to calculate the median.

Table 8 Geochemistry of the magmatic and metamorphic fluid endmembers. Values are in ppm.

The concentrations of Rb, Sn and Cs in muscovite precipitating from the mixed hydrothermal fluid are, besides dependent on the Rb-, Sn- and Cs-content of the mixed fluid, also determined by the $K_{cf,ij}$-values, i.e. the crystal-fluid partition coefficients. Numerical values of these parameters applicable to the magmatic pegmatite-fluid system are not available in literature. Therefore they were calculated for each element with aid of the published values of the fluid-melt partition coefficient, $K_{fm,i}$, and the crystal-melt partition coefficient, $K_{d,ij}$, for muscovite which has been used in the past (e.g. Hulsbosch et al., 2014) and proven to be representative for the system. $K_{cf,ij}$-values were calculated according to the formula: $\mathrm{K_{cf,ij}} = (\mathrm{K_{fm,i}})^{-1} * \mathrm{K_{d,ij}}$ (table 9). Because there is no consensus on the extent of fluid compatibility of Cs in natural as well as experimental set-ups (cf.

Zajacz et al., 2008), the lowest and highest value (assuming Cs is fluid-compatible; i.e. $K_{fm} > 1$) were used in the modelling.

Table 9 Calculations of the fluid-crystal coefficients for Rb, Sn and Cs in muscovite (using the datasets of Adam and Green, 2006; Hu et al., 2008; Icenhower and London, 1995; Zajacz et al., 2008).

The expected Cs-, Sn- and Rb-concentrations in muscovite are calculated for different mixing ratios (figure 12). The value "0" was taken to indicate the pure magmatic signature while "1" represents the metamorphic signature.

Fig. 12 Analyzed quartz vein muscovite (•) versus calculated quartz vein muscovite (x) composition for multiple mixing ratios (Δ). 0 = pegmatitic fluid, 1 = metamorphic fluid.

These calculations show that mixing with a metamorphic fluid explains the Rb- and Sn-concentrations of the quartz vein muscovite. Most quartz vein muscovite samples are enriched in Cs compared to the expected values, even in the case of $K_{fm,Cs} = 1.4$. However, the trend observed in the analytical results is in both cases parallel to the calculated trend. A plausible reason of the relative depletion of Cs in the calculations is that in reality, the $K_{d,Cs\text{-}muscovite}$ (i.e. the compatibility of Cs in muscovite) is higher in Cs-rich systems. Except for this discrepancy in Cs, the process of mixing between a lately exsolved magmatic and a metamorphic fluid is coherent with the observed Rb-Sn-Cs signature in quartz vein muscovite from the Rwamagana-Musha-Ntunga area. The calculations furthermore show that the degree of mixing is highly variable over different quartz veins. The analytical data demonstrates the mixed fluid consists of 20 – 95% of a magmatic fluid and 5 – 80 % of an external (metamorphic) fluid.

Furthermore, fluid mixing can be a major control on the precipitation of Sn-mineralization in hydrothermal quartz veins. In hydrothermal fluids, tin is dominantly transported in the bivalent state as chloride-complex (Migdisov and Williams-Jones, 2005). To precipitate as cassiterite, Sn(II) has to be oxidized to an oxidation state of +IV. A possible reaction mechanism could be (Heinrich, 1990):

$$Sn(II)Cl_x^{2-x} + 2\,H_2O \leftrightarrow Sn(IV)O_2 + 2\,H^+ + x\,Cl^- + H_2\,.$$

This reaction indicates that cassiterite precipitation is favored by any reaction that induces acid neutralization or salinity decrease (Heinrich, 1990). Mixing of a magmatic fluid with preheated meteoric water has been proposed as trigger for Sn- and W-precipitation in quartz veins associated with the Mole Granite, Australia (Audétat et al., 2000b). The low salinity of the metamorphic fluids present in the Rwamagana-Musha-Ntunga area and the deduced high degree of mixing indicates that a salinity decrease of the magmatic fluid certainly can be achieved.

6 Conclusion

The geochemical evolution in the granite-pegmatite-quartz vein system in the Rwamagana-Musha-Ntunga area (East Rwanda) was successfully investigated by muscovite and fluid geochemistry. Trace element content variation in pegmatitic muscovite demonstrates that the pegmatite geochemical evolution can be explained by fractional crystallization. Comparison with the granite-pegmatite system of the Gitarama-Gatumba area (West-Rwanda) indicates that the pegmatites of the Rwamagana-Musha-Ntunga area crystallized from a highly fractionated residual granitic melt.

In previous research, the primary signature of peribatholitic, Sn-bearing quartz veins was often observed to be masked by post-magmatic alteration processes, which complicates the identification of a genetic relationship between granites, pegmatites and quartz veins. Quartz stable isotope data of the Sn-mineralized quartz veins show this is the case for the Rwamagana-Musha-Ntunga area. Therefore, an alternative approach was applied. By analyzing fluid inclusions in quartz from pegmatite bodies, the geochemistry of the primary magmatic fluid could be determined. In combination with the metamorphic fluid endmember signature and muscovite geochemistry, the interaction between these two fluids in the genesis of the peribatholitic, Sn-mineralized quartz veins could be assessed.

Muscovite geochemistry (Rb, Cs and Sn) indicates that exsolution of a magmatic fluid took place relatively late during the fractional crystallization of the pegmatitic melt. The mutual cross-cutting relationships of pegmatites and quartz veins evidence that their emplacement was at least partially contemporaneous. Quantitative simulation of the Rb-Sn-Cs muscovite signature and comparison with the analytical muscovite data confirms that the quartz veins have a mixed magmatic-metamorphic origin. The expected muscovite signature was simulated using fluid-crystal partition coefficients and the mixed fluid geochemistry. The hydrothermal mixed fluid composition was determined by calculating the mixing trend between the magmatic and metamorphic fluids present in the Rwamagana-Musha-Ntunga area and the KAB, as determined by LA-ICP-MS. The simulated trends are parallel with the observed trend, with a slight discrepancy in Cs-content. This deviation is probably caused by using a too low $K_{d,Cs\text{-}muscovite}$. The quantification indicates that the hydrothermal fluid from which the Sn-bearing quartz veins in the Rwamagana-Musha-Ntunga area precipitated consists for 20 – 95 % of a magmatic fluid component and for5 % – 80 % of an external metamorphic fluid component.

Acknowledgments

Johanna Van Daele is a research assistant of the Research Foundation – Flanders (FWO). Research of Niels Hulsbosch is funded by a postdoctoral fellowship of the KU Leuven (2017) and a postdoctoral fellowship of the FWO (2017 – 2020). Field work was supported by a grant from the Dirk Vogel Fund. Additional financial support from the research grant C14/17/056 of the KU Leuven Special Research Fund is acknowledged. Research activity on Sn-W ores of Marie-Christine Boiron is supported by the French National Research Agency through the national program 'Investissements d'avenir' (reference ANR-10-LABX-21–LABEX RESSOURCES21). Dr. Francis Gatare, dr. Emmanuel Munyengabe, dr. Michael Biryabarema and Alain Ntenge of the Rwanda Mines, Petroleum and Gas Board are thanked for the authorization to conduct field work in Rwanda and to export the samples. We wish to thank Mark Thompson, CEO of Piran Resources, Ben Smit, Managing Director, and Rassie Erasmus,

Project Director, for giving us access to the Musha-Ntunga mining area and Didier Kinyaga, Senior Geologist, for the introduction on the geology of the area. We also would like to express our gratitude to dr. Elvira Vassilieva (KU Leuven) for her help with the ICP-OES and ICP-MS analyses and to Herman Nijs (KU Leuven) for preparing the high-quality wafers. We thank editor-in-chief prof. dr. Franco Pirajno and associate editor prof. dr. Kim Hein for the editorial handling of the manuscript. We gratefully acknowledge prof. dr. Olivier Vanderhaeghe and an anonymous reviewer for their careful review and insightful comments that improved the manuscript.

Conflict of interest The authors can confirm that there is no disclosure of potential conflicts of interest, no research involving neither human participants nor animals.

References

Adam, J., Green, T., 2006. Trace element partitioning between mica- and amphibole-bearing garnet lherzolite and hydrous basanitic melt: 1. Experimental results and the investigation of controls on partitioning behaviour. Contrib. to Mineral. Petrol. 152, 1–17. https://doi.org/10.1007/s00410-006-0085-4

Alfonso, P., Melgarejo, J., Yusta, I., Velasco, F., 2003. Geochemistry of feldspars and muscovite in granitic pegmatite from the Cap de Creus pegmatite field, Catalonia, Spain. Can. Mineral. 41, 103–116.

Audétat, A., Günther, D., Heinrich, C.A., 2000a. Magmatic-hydrothermal evolution in a fractionating granite: A microchemical study of the Sn-W-F-mineralized Mole Granite (Australia). Geochim. Cosmochim. Acta 64, 3373–3393. https://doi.org/10.1016/S0016-7037(00)00428-2

Audétat, A., Güther, D., Heinrich, C.A., 2000b. Causes for Large-Scale Metal Zonation around Mineralized Plutons: Fluid Inclusion LA-ICP-MS Evidence from the Mole Granite, Australia. Econ.

Geol. 95, 1563–1581. https://doi.org/10.2113/gsecongeo.95.8.1563

Baker, T., Pollard, P.J., Mustard, R., Markl, G., Graham, J.L., 2005. A comparison of granite-related tin, tungsten, and gold-bismuth deposits: implications for exploration. SEG Newsl. 61, 5–17.

Bakker, R.J., 1997. Clathrates: computer programs to calculate fluid inclusion V-X properties using clathrate melting temperatures. Comput. Geosci. 23, 1–18.

Bakker, R.J., Brown, P.E., 2003. Computer modelling in fluid inclusion research, in: Samson, I.M., Anderson, A., Marshall, D. (Eds.), Fluid Inclusions: Analysis and Interpretation. Mineralogical Association of Canada Short Course Series 32, pp. 175–212.

Baudet, D., Hanon, M., Lemonne, E., Theunissen, K., 1988. Lithostratigraphie du domaine sédimentaire de la chaîne kibarienne au Rwanda. Ann. la société géologique Belgique 112, 225–246.

Beus, A.A., 1986. Geology of Tungsten. UNESCO Publishing.

Boyce, A.J., Fulignati, P., Sbrana, A., 2003. Deep hydrothermal circulation in a granite intrusion beneath Larderello geothermal area (Italy): Constraints from mineralogy, fluid inclusions and stable isotopes. J. Volcanol. Geotherm. Res. 126, 243–262. https://doi.org/10.1016/S0377-0273(03)00150-1

Breiter, K., Ďurišová, J., Hrstka, T., Korbelová, Z., Vašinová Galiová, M., Müller, A., Simons, B., Shail, R.K., Williamson, B.J., Davies, J.A., 2018. The transition from granite to banded aplite-pegmatite sheet complexes: An example from Megiliggar Rocks, Tregonning topaz granite, Cornwall. Lithos 302–303, 370–388. https://doi.org/10.1016/j.lithos.2018.01.010

Brinckmann, J., Lehmann, B., 1983. Exploration de la bastnaésite-moncite dans la région de Gakara, Burundi. Unpubl. report, 157 pp.

Brinckmann, J., Lehmann, B., Hein, U., Höhndorf, A., Mussallam, K., Weiser, T., Timm, F., 2001. La

géologie et la minéralisation primaire de l'or de la Chaîne Kibarienne, nord-ouest du Burundi, Afrique orientale, Bundesanstalt für Geowissenschaften und Rohstoffe.

Brinckmann, J., Lehmann, B., Timm, F., 1994. Proterozoic gold mineralization in NW burundi. Ore Geol. Rev. 9, 85–103. https://doi.org/10.1016/0169-1368(94)90023-X

Cahen, L., Ledent, D., 1979. Précisions sur l'age, la pétrogénèse et la position stratigraphique des granites à étain de l'est de l'Afrique Centrale. Bull. Société Belge Géologique 88, 33–49.

Černý, P., Ercit, T.S., 2005. The Classification of Granitic Pegmatites Revisited. Can. Mineral. 43, 2005–2026. https://doi.org/10.2113/gscanmin.43.6.2005

Černý, P., Meintzer, R.E., Anderson, A.J., 1985. Extreme Fractionation in Rare-Element Granitic Pegmatites: Examples of Data and Mechanisms. Can. Mineral. 23, 381–421.

Černý, P., Teertstra, D.K., Chapman, R., Selway, J.B., Hawthorne, F.C., Ferreira, K., Chackowsky, L.E., Wang, X.-J., Meintzer, R.E., 2012. Extreme Fractionation and Deformation of the Leucogranite – Pegmatite Suite At Red Cross Lake, Manitoba, Canada, IV. Mineralogy. Can. Mineral. 50, 1839–1875.

Chicharro, E., Boiron, M.-C., López-García, J.Á., Barfod, D.N., Villaseca, C., 2016. Origin, ore forming fluid evolution and timing of the Logrosán Sn-(W) ore deposits (Central Iberian Zone, Spain). Ore Geol. Rev. 72, 896–913. https://doi.org/10.1016/j.oregeorev.2015.09.020

Clark, G.S., Černý, P., 1987. Radiogenic 87Sr, its mobility, and the interpretation of RbSr fractionation trends in rare-element granitic pegmatites. Geochim. Cosmochim. Acta 51, 1011–1018. https://doi.org/10.1016/0016-7037(87)90112-8

De Clercq, F., 2012. Metallogenesis of Sn and W vein-type deposits in the Karagwe-Ankole Belt (Rwanda). KU Leuven.

De Clercq, F., Muchez, P., Dewaele, S., Boyce, A., 2008. The tungsten mineralisation at Nyakabingo

and Gifurwe (Rwanda): preliminary results. Geol. Belgica 11, 251–258.

de Kock, G.S., Dhansay, T., Armstrong, R., 2014. Akanyaru-Ankole Supergroup of Rwanda: strata, structures and ages, in: CAG 25. Dar Es Salaam.

Dewaele, S., De Clercq, F., Hulsbosch, N., Piessens, K., Boyce, A., Burgess, R., Muchez, P., 2016a. Genesis of the vein-type tungsten mineralization at Nyakabingo (Rwanda) in the Karagwe–Ankole belt, Central Africa. Miner. Depos. 51, 283–307. https://doi.org/10.1007/s00126-015-0608-x

Dewaele, S., De Clercq, F., Muchez, P., Schneider, J., Burgess, R., Boyce, A., Fernandez Alonso, M., 2010. Geology of the cassiterite mineralisation in the Rutongo area, Rwanda (Central Africa): Current state of knowledge. Geol. Belgica 13, 91–112.

Dewaele, S., Henjes-Kunst, F., Melcher, F., Sitnikova, M., Burgess, R., Gerdes, A., Fernandez-Alonso, M., De Clercq, F., Muchez, P., Lehmann, B., 2011. Late Neoproterozoic overprinting of the cassiterite and columbite-tantalite bearing pegmatites of the Gatumba area, Rwanda (Central Africa). J. African Earth Sci. 61, 10–26. https://doi.org/10.1016/j.jafrearsci.2011.04.004

Dewaele, S., Hulsbosch, N., Cryns, Y., Boyce, A., Burgess, R., Muchez, P., 2016b. Geological setting and timing of the world-class Sn, Nb-Ta and Li mineralization of Manono-Kitotolo (Katanga, Democratic Republic of Congo). Ore Geol. Rev. 72, 373–390. https://doi.org/10.1016/j.oregeorev.2015.07.004

Donnelly, T., Waldron, S., Tait, A., Dougans, J., Bearhop, S., 2001. Hydrogen isotope analysis of natural abundance and deuterium-enriched waters by reduction over chromium on-line to a dynamic dual inlet isotope-ratio mass spectrometer. Rapid Commun. Mass Spectrom. 15, 1297–1303. https://doi.org/10.1002/rcm.361

Duan, Z., Møller, N., Weare, J.H., 1996. A general equation of state for supercritical fluid mixtures and

molecular dynamics simulation of mixture PVTX properties. Geochim. Cosmochim. Acta 60, 1209–1216.

Eldursi, K., Branquet, Y., Guillou-Frottier, L., Marcoux, E., 2009. Numerical investigation of transient hydrothermal processes around intrusions: Heat-transfer and fluid-circulation controlled mineralization patterns. Earth Planet. Sci. Lett. 288, 70–83. https://doi.org/10.1016/j.epsl.2009.09.009

Fehn, U., 1985. Post-magmatic convection related to high heat production in granites of SW England: a theoretical study. Inst. Min. Metall. High Heat, 99–112.

Fernandez-Alonso, M., Cutten, H., De Waele, B., Tack, L., Tahon, A., Baudet, D., Barritt, S.D., 2012. The Mesoproterozoic Karagwe-Ankole Belt (formerly the NE Kibara Belt): The result of prolonged extensional intracratonic basin development punctuated by two short-lived far-field compressional events. Precambrian Res. 216–219, 63–86. https://doi.org/10.1016/j.precamres.2012.06.007

Fernandez-Alonso, M., Tack, L., Tahon, A., 2007. Geological Map of the Mesoproterozoic Northeastern Kibara Belt, 1:500.000.

Frisch, W., 1971. Die Zinn-Wolfram-Provinz in Rwanda (Zentral-Afrika). Erzmetall 24, 593–600.

Fyfe, W.S., Price, N.J., Thompson, A.B., 1978. Fluids in the earth's crust. Elsevier Scientific Publishing Company, Amsterdam.

Gérards, J., Ledent, D., 1970. Grands traits de la géologie du Rwanda, différents types de roches granitiques et premières données sur les âges de ces roches. Ann. la société géologique Belgique 93, 477–489.

Gleeson, S.A., Roberts, S., Fallick, A.E., Boyce, A.J., 2008. Micro-Fourier Transform Infrared (FT-IR) and δD value investigation of hydrothermal vein quartz: Interpretation of fluid inclusion δD values in

hydrothermal systems. Geochim. Cosmochim. Acta 72, 4595–4606. https://doi.org/10.1016/j.gca.2008.06.014

Goldstein, R.H., Reynolds, T.J., 1994. Systematics of fluid inclusions in diagenetic minerals. SEPM.

Guillong, M., Meier, D., Allan, M.M., Heinrich, C.A., Yardley, B.W.D., 2008. Appendix A6: SILLS: a MATLAB-based program for the reduction of laser ablation ICP-MS data of homogeneous materials and inclusions, in: Sylvester, P. (Ed.), Laser Ablation ICP-MS in the Earth Sciences: Current Practices and Outstanding Issues. Mineralogical Association of Canada Short Course, Vancouver, B.C.

Hanon, M., Rusanganwa, J., 1991. Carte Géologique du Rwanda, Feuille Kigali, 1:100,000 et note explicative. Département de Géologie et de Minéralogie du Musée royal de l'Afrique Centrale et le Ministère de l'Industrie et de l'Artisanat du Rwanda.

Harlaux, M., Mercadier, J., Bonzi, W.M., Kremer, V., Marignac, C., Cuney, M., 2017. Geochemical Signature of Magmatic-Hydrothermal Fluids exsolved from the Beauvoir Rare-Metal Granite (Massif Central , France): Insights from LA-ICPMS Analysis of Primary Fluid Inclusions. Geofluids 1–26. https://doi.org/10.1155/2017/1925817

Haynes, F.M., 1985. Determination of fluid inclusion compositions by sequential freezing. Econ. Geol. 80, 1436–1439.

Heinrich, C.A., 1990. The chemistry of hydrothermal tin(-tungsten) ore deposition. Econ. Geol. 85, 457–481. https://doi.org/10.2113/gsecongeo.85.3.457

Hoefs, J., 2015. Stable isotope geochemistry, Seventh. ed. Springer. https://doi.org/10.1007/978-3-319-19716-6

Hu, X., Bi, X., Hu, R., Shang, L., Fan, W., 2008. Experimental study on tin partition between granitic silicate melt and coexisting aqueous fluid. Geochem. J. 42, 141–150.

https://doi.org/10.2343/geochemj.42.141

Hulsbosch, N., 2018. Nb-Ta-Sn-W distribution in granite-related ore systems: fractionation mechanisms and examples from the Karagwe-Ankole Belt of Central Africa, in: Decrée, S., Robb, L. (Eds.), Ore Deposits Origin Exploration and Exploitation. Wiley.

Hulsbosch, N., 2016. Chemical fractionation in granite-related ore systems - Evidence from Nb-Ta-Sn pegmatite-type and Sn-W quartz vein-type mineralisation in the Karagwe-Ankole Belt (Rwanda). Unpublished PhD-thesis, KU Leuven.

Hulsbosch, N., Boiron, M.-C., Dewaele, S., Muchez, P., 2016. Fluid fractionation of tungsten during granite–pegmatite differentiation and the metal source of peribatholitic W quartz veins: Evidence from the Karagwe-Ankole Belt (Rwanda). Geochim. Cosmochim. Acta 175, 299–318. https://doi.org/10.1016/j.gca.2015.11.020

Hulsbosch, N., Hertogen, J., Dewaele, S., Andre, L., Muchez, P., 2013. Petrographic and mineralogical characterisation of fractionated pegmatites culminating in the Nb-Ta-Sn pegmatites of the Gatumba area (western Rwanda). Geol. Belgica 16, 105–117.

Hulsbosch, N., Hertogen, J., Dewaele, S., André, L., Muchez, P., 2014. Alkali metal and rare earth element evolution of rock-forming minerals from the Gatumba area pegmatites (Rwanda): Quantitative assessment of crystal-melt fractionation in the regional zonation of pegmatite groups. Geochim. Cosmochim. Acta 132, 349–374. https://doi.org/10.1016/j.gca.2014.02.006

Hulsbosch, N., Van Daele, J., Reinders, N., Dewaele, S., Jacques, D., Muchez, P., 2017. Structural control on the emplacement of contemporaneous Nb-Ta-Sn pegmatite intrusions and Sn quartz veins: insights from the Musha and Ntunga deposits of the Karagwe-Ankole Belt, Rwanda. J. African Earth Sci. 137, 24–32.

Icenhower, J., London, D., 1995. An experimental study of element partitioning among biotite,

muscovite, and coexisting peraluminous silicic melt at 200 MPa (H2O). Am. Mineral. 80, 1229–1251.

Jolliff, B.L., Papike, J.J., Shearer, C.K., 1992. Petrogenetic relationships between pegmatite and granite based on geochemistry of muscovite in pegmatite wall zones, Black Hills, South Dakota, USA. Geochim. Cosmochim. Acta 56, 1915–1939. https://doi.org/http://dx.doi.org/10.1016/0016-7037(92)90320-I

Kelly, W.C., Rye, R.O., 1979. Geologic, fluid inclusion, and stable isotope studies of the tin-tungsten deposits of Panasqueira, Portugal. Econ. Geol. 74, 1721–1822. https://doi.org/10.2113/gsecongeo.74.8.1721

Kozlik, M., Raith, J.G., Gerdes, A., 2016. U-Pb, Lu-Hf and trace element characteristics of zircon from the Felbertal scheelite deposit (Austria): New constraints on timing and source of W mineralization. Chem. Geol. 421, 112–126. https://doi.org/10.1016/j.chemgeo.2015.11.018

Legros, H., Marignac, C., Mercadier, J., Cuney, M., Richard, A., Wang, R.C., Charles, N., Lespinasse, M.Y., 2016. Detailed paragenesis and Li-mica compositions as recorders of the magmatic-hydrothermal evolution of the Maoping W-Sn deposit (Jiangxi, China). Lithos 264, 108–124. https://doi.org/10.1016/j.lithos.2016.08.022

Lehmann, B., Halder, S., Ruzindana Munana, J., de la Paix Ngizimana, J., Biryabarema, M., 2014. The geochemical signature of rare-metal pegmatites in Central Africa: Magmatic rocks in the Gatumba tin–tantalum mining district, Rwanda. J. Geochemical Explor. 144, 528–538. https://doi.org/10.1016/j.gexplo.2013.11.012

Lehmann, B., Nakai, S., Höhndorf, A., Brinckmann, J., Dulski, P., Hein, U.F., Masuda, A., 1994. REE mineralization at Gakara, Burundi: Evidence for anomalous upper mantle in the western Rift Valley. Geochim. Cosmochim. Acta 58, 985–992. https://doi.org/10.1016/0016-7037(94)90520-7

Leisen, M., Dubessy, J., Boiron, M.-C., Lach, P., 2012. Improvement of the determination of element concentrations in quartz-hosted fluid inclusions by LA-ICP-MS and Pitzer thermodynamic modeling of ice melting temperature. Geochim. Cosmochim. Acta 90, 110–125.

London, D., 2005. Geochemistry of alkali and alkaline earth elements in ore-forming granites, pegmatites, and rhyolites, in: Linnen, R., Sampson, I. (Eds.), Rare-Element Geochemistry of Ore Deposits, GAC Short Course Notes 17. pp. 17–43.

Longerich, H.P., Jackson, S.E., Günther, D., 1996. Laser ablation inductivel coupled plasma mass spectrometric transient signal data aqcuisition and analyte concentration calculation. J. Anal. At. Spectrom. 11, 899–904.

Marignac, C., Cathelineau, M., 2010. The Nature of Ore-forming Fluids in Peri-Batholitic Sn-W Deposits and a Classification. James Cook Univ, Townsville.

Marsala, A., Wagner, T., Wälle, M., 2013. Late-metamorphic veins record deep ingression of meteoric water: A LA-ICPMS fluid inclusion study from the fold-and-thrust belt of the Rhenish Massif, Germany. Chem. Geol. 351, 134–153. https://doi.org/10.1016/j.chemgeo.2013.05.008

Martins, T., Roda-Robles, E., Lima, A., De Parseval, P., 2012. Geochemistry and evolution of micas in the Barroso-Alvão pegmatite field, Northern Portugal. Can. Mineral. 50, 1117–1129. https://doi.org/10.3749/canmin.50.4.1117

Matsuhisa, Y., Goldsmith, J.R., Clayton, R.N., 1979. Oxygen isotopic fractionation in the system quartz-albite-anorthite-water. Geochim. Cosmochim. Acta 43, 1131–1140. https://doi.org/10.1016/0016-7037(79)90099-1

Melcher, F., Graupner, T., Gäbler, H.-E., Sitnikova, M., Henjes-Kunst, F., Oberthür, T., Gerdes, A., Dewaele, S., 2015. Tantalum–(niobium–tin) mineralisation in African pegmatites and rare metal granites: Constraints from Ta–Nb oxide mineralogy, geochemistry and U–Pb geochronology.

Ore Geol. Rev. 64, 667–719. https://doi.org/10.1016/j.oregeorev.2013.09.003

Melcher, F., Graupner, T., Gäbler, H.E., Sitnikova, M., Oberthür, T., Gerdes, A., Badanina, E., Chudy, T., 2016. Mineralogical and chemical evolution of tantalum-(niobium-tin) mineralisation in pegmatites and granites. Part 2: Worldwide examples (excluding Africa) and an overview of global metallogenetic patterns. Ore Geol. Rev. in press. https://doi.org/10.1016/j.oregeorev.2016.03.014

Migdisov, A.A., Williams-Jones, A.E., 2005. An experimental study of cassiterite solubility in HCl-bearing water vapour at temperatures up to 350 °C. Implications for tin ore formation. Chem. Geol. 217, 29–40. https://doi.org/10.1016/j.chemgeo.2004.11.018

Monteyne-Poulaert, G., Delwiche, R., Safianikoff, A., Cahen, L., 1962. Age de minéralisations pegmatitiques et filoniennes du Rwanda et du Burundi. Ann. la société géologique Belgique 71, 272–295.

Muchez, P., Marshall, J.D., Touret, J.L., Viaene, W., 1994. Origin and migration of paleofluids in the Upper Visean of the Campine Basin, northern Belgium. Sedimentology 41, 133–145.

Neiva, A.M.R., 1987. Geochemistry of white micas from Portuguese tin and tungsten deposits. Chem. Geol. 63, 299–317. https://doi.org/10.1016/0009-2541(87)90168-9

Neumann, H., Mead, J., Vitaliano, C.J., 1954. Trace element variation during fractional crystallization as calculated from the distribution law. Geochim. Cosmochim. Acta 6, 90–99.

Oyarzábal, J., Galliski, M.Á., Perino, E., 2009. Geochemistry of K-feldspar and muscovite in rare-element pegmatites and granites from the Totoral pegmatite field, San Luis, Argentina. Resour. Geol. 59, 315–329. https://doi.org/10.1111/j.1751-3928.2009.00100.x

Passchier, C.W., Trouw, R.A.J., 2005. Micro-tectonics. Springer Verlag, Berlin-Heidelberg.

Patterson, D.J., Ohmoto, H., Solomon, M., 1981. Geologic setting and genesis of cassiterite-sulfide

mineralization at renison bell, western Tasmania-a discussion. Econ. Geol. 76, 393–438. https://doi.org/10.2113/gsecongeo.77.1.199

Pettke, T., Oberli, F., Audétat, A., Guillong, M., Simon, A.C., Hanley, J.J., Klemm, L.M., 2012. Recent developments in element concentration and isotope ratio analysis of individual fluid inclusions by laser ablation single and multiple collector ICP-MS. Ore Geol. Rev. 44, 10–38. https://doi.org/10.1016/j.oregeorev.2011.11.001

Pichavant, M., Manning, D., 1984. Petrogenesis of tourmaline granites and topaz granites; the contribution of experimental data. Phys. Earth Planet. Inter. 35, 31–50. https://doi.org/10.1016/0031-9201(84)90032-3

Piessens, K., Muchez, P., 2009. Calibrating the confocal micro-Raman spectrometer at the GSB-RBINS for quantifying the composition of Raman active components in fluid inclusions, in: Third International Conference Geologica Belgica. Challenges for the Planet: Earth Sciences' Perspective. Gent (Belgium), pp. 83–84.

Pohl, W., 1994. Metallogeny of the northeastern Kibara belt, Central Africa—Recent perspectives. Ore Geol. Rev. 9, 105–130. https://doi.org/10.1016/0169-1368(94)90024-8

Polya, D.A., Foxford, K.A., Stuart, F., Boyce, A., Fallick, A.E., 2000. Evolution and paragenetic context of low δD hydrothermal fluids from the Panasqueira W-Sn deposit, Portugal: New evidence from microthermometric, stable isotope, noble gas and halogen analyses of primary fluid inclusions. Geochim. Cosmochim. Acta 64, 3357–3371. https://doi.org/10.1016/S0016-7037(00)00459-2

Prochaska, W., Mogessie, A., Raith, J.G., 1992. Formation of the talc deposit of Kibanda (Rwanda) and its relation to the regional metamorphic evolution Volcanic rocks Granites and gneisses Granitized zone Location of the talc. J. African Earth Sci. 14, 499–509.

Rauchenstein-Martinek, K., Wagner, T., Wälle, M., Heinrich, C.A., Arlt, T., 2016. Chemical evolution of metamorphic fluids in the Central Alps, Switzerland: insight from LA-ICPMS analysis of fluid inclusions. Geofluids 16, 877–908. https://doi.org/10.1111/gfl.12194

Reinders, N., 2016. Metallogenic study of the Musha-Ntunga Nb-Ta-Sn pegmatite and Sn vein-type deposits, Central Rwanda. Unpublished masterthesis, KU Leuven.

Roda-Robles, E., Pesquera, A., Gil-Crespo, P., Torres-Ruiz, J., 2012. From granite to highly evolved pegmatite: A case study of the Pinilla de Fermoselle granite–pegmatite system (Zamora, Spain). Lithos 153, 192–207. https://doi.org/10.1016/j.lithos.2012.04.027

Roda-Robles, E., Pesquera Perez, A., Velasco Roldan, F., Fontan, F., 1999. The granitic pegmatites of the Fregeneda area (Salamanca, Spain): characteristics and petrogenesis. Mineral. Mag. 63, 535–558.

Romer, R.L., Lehmann, B., 1995. U-Pb columbite age of Neoproterozoic Ta-Nb mineralization in Burundi. Econ. Geol. 90, 2303–2309. https://doi.org/10.2113/gsecongeo.90.8.2303

Saleh, G.M., El Galy, M.M., Obeid, M.A., 2008. Geochemical characteristics and spectrometric prospecting in the muscovite-bearing pegmatites and granites, southeastern Aswan, Egypt. Chinese J. Geochemistry 27, 9–20. https://doi.org/10.1007/s11631-008-0009-2

Sharp, Z.D., 1990. A laser-based microanalytical method for the in situ determination of oxygen isotope ratios of silicates and oxides. Geochim. Cosmochim. Acta 54, 1353–1357. https://doi.org/10.1016/0016-7037(90)90160-M

Sheppard, S.M.F., 1986. Characterization and isotopic variations in natural waters, in: Valley, J.W., Taylor, H.P.J., O'Neil, J.R. (Eds.), Stable Isotopes in High Temperature Geological Processes. pp. 49–60.

Smeds, S.A., 1992. Trace elements in potassium-feldspar and muscovite as a guide in the prospecting

for lithium- and tin-bearing pegmatites in Sweden. J. Geochemical Explor. 42, 351–369. https://doi.org/10.1016/0375-6742(92)90032-4

Suhr, N., Ingamells, C., 1966. Solution technique for the analysis of silicates. Anal. Chem. 38, 730–734.

Tack, L., Liégeois, J.P., Deblond, a., Duchesne, J.C., 1994. Kibaran A-type granitoids and mafic rocks generated by two mantle sources in a late orogenic setting (Burundi). Precambrian Res. 68, 323–356. https://doi.org/10.1016/0301-9268(94)90036-1

Tack, L., Wingate, M.T.D., De Waele, B., Meert, J., Belousova, E., Griffin, B., Tahon, A., Fernandez-Alonso, M., 2010. The 1375 Ma "Kibaran event" in Central Africa: Prominent emplacement of bimodal magmatism under extensional regime. Precambrian Res. 180, 63–84. https://doi.org/10.1016/j.precamres.2010.02.022

Taylor, R.G., 1979. Geology of tin deposits. Elsevier, Amsterdam, Oxford and New York.

Tindle, A.G., 2001. Structural Formula Calculators (Excel format) - Muscovite [WWW Document]. URL http://www.open.ac.uk/earth-research/tindle/AGT/AGT_Home_2010/Microprobe-2.html (accessed 5.18.16).

Tindle, A.G., Webb, P.C., 1990. Estimation of lithium contents in trioctahedral micas using microprobe data: application to micas from granitic rocks. Eur. J. Mineral. 2, 595–610. https://doi.org/10.1127/ejm/2/5/0595

Tischendorf, G., Gottesmann, B., Förster, H.-J., Trumbull, R.B., 1997. On Li-bearing Micas: Estimating Li from Electron Microprobe Analyses and an Improved Diagram for Graphical Representation. Mineral. Mag. 61, 809–834. https://doi.org/10.1180/minmag.1997.061.409.05

Van Daele, J., 2016. Regional variation of and controls on the granite-related Nb-Ta-Sn deposits in the Rwamagana-Musha-Ntunga area, East Rwanda. Unpublished masterthesis KU Leuven.

Van Lichtervelde, M., Grégoire, M., Linnen, R.L., Béziat, D., Salvi, S., 2008. Trace element geochemistry by laser ablation ICP-MS of micas associated with Ta mineralization in the Tanco pegmatite, Manitoba, Canada. Contrib. to Mineral. Petrol. 155, 791–806. https://doi.org/10.1007/s00410-007-0271-z

Varlamoff, N., 1972. Central and West African Rare-Metal Granitic Pegmatites, Related Aplites, Quartz veins and Mineral Deposits. Miner. Depos. 7, 202–216.

Varlamoff, N., 1969. Transitions entre les filons de quartz et les pegmatites stannifères de la régian de Musha-Ntunga (Rwanda). Ann. la société géologique Belgique 92, 193–213.

Verbovsek, T., 2011. A comparison of parameters below the limit of detection in geochemical analyses by substitution methods. RMZ – Mater. Geoenvironment 58, 393–404.

Vertriest, W., 2014. Petrographical, mineralogical and geochemical study of the Nb-Ta and Sn mineralisations of Musha-Ntunga (Rwanda). KU Leuven.

Viana, R.R., Jordt-Evangelista, H., Stern, W.B., 2007. Geochemistry of muscovite from pegmatites of the Eastern Brazilian pegmatite province: a clue to petrogenesis and mineralization potential. Eur. J. Mineral. 19, 745–755. https://doi.org/10.1127/0935-1221/2007/0019-1760

Vieira, R., Roda-Robles, E., Pesquera, A., Lima, A., 2011. Chemical variation and significance of micas from the Fregeneda-Almendra pegmatitic field (Central-Iberian Zone, Spain and Portugal). Am. Mineral. 96, 637–645. https://doi.org/10.2138/am.2011.3584

Wilkinson, J.J., 1990. The role of metamorphic fluids in the development of the Cornubian orefield: fluid inclusion evidence from south Cornwall. Mineral. Mag. 54, 219–230. https://doi.org/10.1180/minmag.1990.054.375.08

Williamson, B.J., Müller, A., Shail, R.K., 2010. Source and partitioning of B and Sn in the Cornubian batholith of southwest England. Ore Geol. Rev. 38, 1–8.

https://doi.org/10.1016/j.oregeorev.2010.05.002

Wise, M.A., Brown, C.D., 2010. Mineral chemistry, petrology and geochemistry of the Sebago granite-pegmatite system, Southern Maine, USA. J. Geosci. 55, 3–26. https://doi.org/10.3190/jgeosci.061

Wood, S.A., Samson, I.M., 2000. The hydrothermal geochemistry of tungsten in granitoid environments: I. Relative solubilities of ferberite and scheelite as a function of T, P, pH, and m(NaCl). Econ. Geol. 95, 143–182. https://doi.org/10.2113/gsecongeo.95.1.143

Zajacz, Z., Halter, W.E., Pettke, T., Guillong, M., 2008. Determination of fluid/melt partition coefficients by LA-ICPMS analysis of co-existing fluid and silicate melt inclusions: Controls on element partitioning. Geochim. Cosmochim. Acta 72, 2169–2197. https://doi.org/10.1016/j.gca.2008.01.034

Zhang, R.-Q., Sun, W. -d., Lehmann, B., 2016. Multiple tin mineralization events in Africa: Constraints by in-situ LA-ICPMS cassiterite U-PB ages, in: 35th International Geological Congress Cape Town, South Africa.

Appendix

Table A.1 Major element composition of Rwamagana-Musha-Ntunga muscovite samples. All values are in wt%. H_2O is calculated stoechiometrically according to Tindle and Webb (1990).

Figure captions

Fig. 1 Schematic diagram illustrating primary granite-related W-Sn deposit styles in combination with their type-localities (1: North American Cordillera, 2: Bolivian province, 3: Iberian – Panasqueira province, 4: French Massif Central, 5: Cornwall, 6: Erzgebirge/Krušné Hory, 7: Kibara Metallogenic province, 8: southeast China province, 9: Myanmar-Thailand-Maleysia and 10: east Australian province). Styles partly after Baker et al. (2005). W-Sn province locations after Taylor (1979) and Beus (1986), Nb-Ta-Sn provinces after Melcher et al. (2016). Figure from Hulsbosch (2016).

Fig. 2 Distribution of lithological groups, granite intrusions and Nb-Ta-Sn-W mineralization in Rwanda. 1 = Rwamagana city, 2 = Musha-Ntunga, 3 = Kigali city, 4 = Nyakabingo, 5 = Rutongo, 6 = Gatumba, 7 = Kibuye city. The Rwamagana-Musha-Ntunga study area is indicated with the blue rectangle. Modified after Fernandez-Alonso et al. (2007).

Fig. 3 Geological map of the Rwamagana-Musha-Ntunga area with indication of pegmatite and quartz vein occurrence (after Hanon and Rusanganwa, 1991; Hulsbosch et al., 2017).

Fig. 4 Petrography of the pegmatites and quartz veins: a) pegmatite (mu = muscovite, qz = quartz, kaol kaolinite, fsp = feldspar), b) pegmatite crosscutting quartz vein with muscovite rim, c) folded metamorphic quartz vein perpendicular to the bedding, d) inset of c), quartz vein deflects host rock axial planar cleavage, e) bedding-parallel, metamorphic quartz vein with biotite-garnet rim, indicated in red.

Fig. 5 $\delta^{18}O$ – δD plot of the calculated and analyzed isotopic composition of the fluids present in the Sn-bearing quartz veins in the Rwamagana-Musha-Ntunga area. The global meteoric water line and the ranges of metamorphic water, magmatic water and water that interacted with organic matter are indicated for comparison (cf. Hoefs, 2015; Sheppard, 1986).

Fig. 6 Trace element concentrations of muscovite samples of the Rwamagana-Musha-Ntunga area. A distinction between non-mineralized and mineralized pegmatites and quartz veins is given.

Fig. 7 (A) and (B) fluid inclusions in magmatic quartz, (C) coarsely crystallized melt inclusion in magmatic quartz, (D) fluid inclusions in metamorphic quartz.

Fig. 8 Fluid inclusion LA-ICP-MS data of magmatic and metamorphic quartz, from the RMN and Kibuye area, respectively. Samples with one of the parameters below the detection limit were given an arbitrary value of 1 ppm for that element to display them in the log-log diagrams.

Fig. 9 LA-ICP-MS spectra of two fluid inclusions in magmatic and metamorphic quartz, from the RMN and Kibuye area, respectively.

Fig. 10 Comparison of Rwamagana-Musha-Ntunga muscovite samples of this study with the pegmatitic muscovite zonation model of Gitarama-Gatumba of Hulsbosch et al. (2014) and the Nyakabingo quartz vein muscovite samples of Hulsbosch et al. (2016). *F* represents the fraction of the melt that crystallized.

Fig. 11 Conceptual representation of (a) the expected muscovite signature, (b) the expected fluid signature and (c) the geological situation in case of early (1), intermediate (2) and late (3) exsolution and subsequent mixing.

Fig. 12 Analyzed quartz vein muscovite (•) versus calculated quartz vein muscovite (x) composition for multiple mixing ratios (Δ). 0 = pegmatitic fluid, 1 = metamorphic fluid.

.

Table 1 Pegmatite and quartz vein mineralogy in the Rwamagana-Musha-Ntunga area (Varlamoff, 1969).

Type*	Mineralogical description
A	Pegmatite dyke with microcline, graphic feldspar-quartz, quartz, biotite, muscovite and schorl.
B	Pegmatite dyke with microcline, graphic feldspar-quartz, quartz, muscovite and tourmaline.
C	Partly albitised pegmatite dyke with microcline, quartz, and muscovite.
D	Albitised pegmatite dyke with microcline, muscovite, amblygonite, spodumene, columbite-tantalite, traces of cassiterite and a quartz-muscovite core zone
E	Intensely albitised pegmatite dyke with muscovite, lepidolite, spodumene, beryl, columbite-tantalite and traces of microcline.
F	Quartz vein with quartz, feldspar, muscovite and cassiterite

* Varlamoff (1969)

Table 2 Stable isotope data of Sn-bearing quartz vein samples from the Rwamagana-Musha-Ntunga area. All values are in ‰ V-SMOW.

	δ^{18}O V-SMOW (quartz)	δ^{18}O V-SMOW (fluid, at 350 °C)	δD V-SMOW (water)
MN13VW13	14.9	9.6	-29.5
MN13VW21	14.6	9.3	-59.7
MN13VW23	14.7	9.4	-43.4
MN13VW32	14.7	9.4	-45.2
MN13VW33	15.2	9.9	-45.5
MN13VW35	13.8	8.5	-27.6
MN13VW37	14.3	9.0	-39.8
MN13VW39	15.8	10.5	-39.2
MN13VW41	13.1	7.8	-28.6

all values are in ‰ V-SMOW

Table 3 Trace element concentrations of Rwamagana-Musha-Ntunga muscovite samples. All values are in ppm.

	03J	19J	23J	44J	47J	49J	52J	53J	62J	67J	08N
	P	P	P	P	P	P	P	P	P	P	P
Ba	16	30	41	58	83	23	12	14	100	162	24
Cs	225	67	96	82	88	348	291	212	110	/	359
K	83461	79570	83125	85919	86947	84343	84182	83192	84883	82120	79133
Li	924	1168	1987	117	110	582	392	452	1837	/	170
Nb	176	170	177	91	85	187	252	216	106	/	122
Rb	3046	1693	2368	2482	2699	5027	4464	4040	1771	1967	5337
Sn	345	121	231	531	467	466	410	428	212	360	482
Sr	11	8	10	11	13	18	15	14	11	10	20
Ta	29	10	15	68	72	44	27	22	11	/	48
W	6	17	8	3	3	4	2	2	7	/	2
Zn	432	272	536	182	194	893	385	557	388	62	132

	17N	35N	37N	39N	50N	51N	54N	57N	17J	58J	59J
	P	P	P	P	P	P	P	P	Q	Q	Q
Ba	305	185	79	91	51	173	24	22	130	2249	746
Cs	248	334	384	302	335	350	417	1180	62	157	/
K	82758	73008	82393	76237	84562	80327	81250	79939	81531	75340	78971
Li	575	556	465	780	444	431	387	288	1143	455	/
Nb	56	94	91	66	52	80	49	76	113	71	/
Rb	1462	2624	4056	3958	3376	3888	3647	8743	813	482	620
Sn	431	419	461	388	456	429	555	811	87	411	659
Sr	45	13	17	15	13	17	13	33	6	86	52
Ta	19	45	63	60	49	54	70	104	16	2	/
W	2	3	2	2	2	2	2	1	7	10	/
Zn	127	163	300	249	237	222	187	126	151	38	38

	69J	07N	21N	32N	45N	52aN	52bN	58N	62N	64N	66N
	Q	Q	Q	Q	Q	Q	Q	Q	Q	Q	Q
Ba	51	1552	638	531	530	22	574	355	2431	/	228
Cs	100	146	356	116	/	/	384	150	336	405	/
K	84171	71598	83669	82671	81574	81445	80376	82808	77704	83277	71410
Li	1673	116	857	1038	/	/	1517	429	646	835	/
Nb	109	41	69	19	/	/	64	40	82	76	/
Rb	1648	749	1732	531	1748	3777	1496	595	2362	2383	610
Sn	213	579	527	237	749	586	680	556	696	689	549
Sr	8	44	66	76	37	13	45	58	44	45	55
Ta	11	3	60	6	/	49	54	7	18	13	/

W	7	3	6	5	/	2	2	4	9	7	/
Zn	382	41	122	47	181	192	147	39	77	89	39

P = pegmatitic muscovite, Q = quartz vein muscovite, / = not analyzed

Table 4 Microthermometric data of the H_2O-CO_2-N_2-NaCl fluid inclusions in magmatic quartz.

Name	V_{gas}	T_m CO_2	T_{fm}	T_m ice	T_m clath	T_h CO_2	T_h tot	Mass % NaCl
1	65	-59.1	-22.6	-6.4	8.4	30.8	302	12.6
2	67	-57.7	-22.6	-7.3	8.4	30.3	301	12.5
3	65	-59.2	-21.9	-7.3	8.4	30.3	302	12.5
4	65	-58.8	-21.9	-7.2	7.9	30.1	301	12.7
5	66	-58.9	-22.6	-7.5	8.5	30.3	304	12.6
6	66	-58.7	-26.1	-7.6	8.3	30.1	305	12.9
7	65	-59.1	-24.6	-7.1	8.4	31.1	312	12.6
8	68	-59.1	-24.6	-8.0	8.0	30.3	301	14.4
9	68	-59.1	-24.6	-7.6	8.6	31.2	299	11.8
10	67	-59.1	-24.6	-8.0	8.2	30.8	304	13.5
11	66	-58.8	-21.1	-8.1	8.3	30.1	304	12.9
12	65	-59.2	-21.7	-7.7	8.4	30.8	304	12.6
13	67	-59.2	-22.8	-7.3	8.3	30.1	304	12.9
14	68	-59.2	-22.8	-7.2	8.4	30.8	301	12.6
15	68	-58.9	-23.8	-7.5	7.9	30.1	302	12.7
16	64	-59.1	-23.8	-7.1	8.5	30.3	301	12.6
17	63	-59.1	-23.8	-7.6	8.3	30.1	304	12.9
18	60	-58.8	-22.6	-7.1	8.3	30.1	303	12.9
19	64	-58.9	-26.1	-8.0	8.4	30.8	302	12.6
20	66	-59.1	-22.6	-8.7	8.4	30.3	301	12.6
21	67	-58.1	-22.6	-6.4	8.4	30.8	308	12.6
22	67	-59.1	-22.6	-7.3	7.9	30.1	301	12.7
23	64	-58.8	-21.9	-7.3	8.4	30.8	301	12.6
24	65	-59.1	-22.6	-7.3	8.3	30.1	301	12.9
25	64	-59.1	-23.4	-7.2	7.9	30.1	302	12.7
26	63	-59.1	-23.5	-7.5	8.3	30.1	302	12.9
27	63	-59.1	-22.1	-7.6	8.3	30.1	302	12.9
28	68	-58.8	-21.1	-7.1	8.4	30.8	304	12.6
29	67	-58.8	-24.6	-6.8	7.9	30.1	306	12.7
30	66	-59.1	-22.6	-8.5	8.4	30.8	306	12.6
31	65	-58.8	-23.6	-7.1	8.0	29.8	303	11.8
32	66	-59.0	-24.7	-7.7	8.3	30.1	304	12.2

33	59	-58.9	-25.0	-7.7	8.2	30.0	302	11.9
34	66	-58.8	-22.1	-7.3	8.6	30.6	304	13.1
35	69	-58.6	-22.0	-6.8	8.3	30.2	301	13.0
36	60	-59.3	-24.7	-6.9	8.4	29.9	303	12.9
37	60	-58.9	-23.9	-7.4	8.4	30.4	309	12.7
38	59	-58.5	-21.4	-7.4	8.3	30.5	302	13.0
39	61	-59.1	-25.5	-7.0	8.6	29.6	300	12.7
40	68	-59.2	-22.8	-7.3	8.1	30.6	304	12.0
41	63	-58.8	-22.8	-7.7	8.5	30.7	303	12.1
42	65	-58.9	-22.4	-7.6	8.2	30.6	300	13.0
43	62	-58.8	-20.8	-8.0	8.4	30.5	304	12.6
44	59	-59.0	-22.3	-7.4	8.3	30.0	302	13.0
45	58	-58.9	-22.0	-7.7	8.0	30.2	303	13.0
46	63	-58.5	-24.9	-8.0	8.3	30.9	303	13.3
47	69	-58.9	-22.1	-7.7	8.6	30.8	303	12.7
48	71	-58.9	-22.5	-7.8	8.6	30.2	301	12.2
49	65	-59.5	-24.6	-7.6	8.3	30.9	300	12.7
50	63	-58.3	-20.2	-8.4	8.6	30.5	302	11.9
51	65	-58.8	-23.0	-6.9	8.0	30.5	302	12.1
52	69	-59.1	-23.3	-8.5	8.1	30.9	302	12.7

Table 5 Microthermometric data of the H_2O-CO_2-(N_2)-NaCl fluid inclusions in metamorphic quartz.

Name	V_{gas}	T_m CO_2	T_{fm}	T_m ice	T_m clath	T_h CO_2	T_h tot	Mass % NaCl
1	57	-57.3	n.o.	-3.7	8.2	27.3	n.d.	5.9
2	55	-57.1	n.o.	-3.3	9.1	29.0	n.d.	4.3
3	56	-56.9	n.o.	-3.3	9.1	29.4	n.d.	4.3
4	57	-56.9	n.o.	-3.3	9.1	29.1	n.d.	4.3
5	55	-57.0	n.o.	-4.0	9.1	29.2	n.d.	4.3
6	57	-57.0	n.o.	-4.0	9.1	29.2	n.d.	4.3
7	57	-56.9	n.o.	-3.7	9.1	29.1	n.d.	4.3
8	53	-57.0	n.o.	-3.3	9.0	29.1	n.d.	4.5
9	55	-56.9	n.o.	-4.1	9.3	28.9	n.d.	3.9
10	54	-57.1	n.o.	-4.0	9.2	29.3	n.d.	4.1
11	51	-56.9	n.o.	-3.3	9.2	28.9	n.d.	4.1
12	57	-57.1	n.o.	-3.3	9.2	29.1	n.d.	4.1
13	55	-56.9	n.o.	-3.4	9.2	29.5	n.d.	4.1
14	53	-57.0	n.o.	-3.6	9.1	29.1	n.d.	4.3
15	58	-56.9	n.o.	-3.3	9.1	28.9	n.d.	4.3
16	54	-57.0	n.o.	-3.7	9.2	28.9	n.d.	4.1
17	52	-57.0	n.o.	-3.8	8.9	29.1	n.d.	4.6

18	52	-56.9	n.o.	-3.3	9.1	29.1	n.d.	4.3
19	55	-56.9	n.o.	-3.3	9.1	28.9	n.d.	4.3
20	56	-57.0	n.o.	-3.5	9.1	28.9	n.d.	4.3
21	52	-56.9	n.o.	-3.4	9.1	29.0	n.d.	3.9
22	55	-56.5	n.o.	-3.7	8.7	28.7	n.d.	3.8
23	54	-57.3	n.o.	-3.3	9.1	30.0	n.d.	3.9
24	55	-56.9	n.o.	-3.3	9.3	28.6	n.d.	4.3
25	55	-57.0	n.o.	-3.4	8.7	29.1	n.d.	5.0
26	54	-57.1	n.o.	-3.3	9.0	29.6	n.d.	4.7
27	54	-57.1	-32	-3.3	8.8	30.1	n.d.	3.8
28	55	-56.9	n.o.	-3.9	9.2	29.7	n.d.	4.9
29	54	-57.1	n.o.	-2.4	8.9	28.9	n.d.	4.3
30	56	-57.0	n.o.	-3.4	8.8	28.7	n.d.	4.0
31	53	-57.3	n.o.	-4.0	8.9	29.1	n.d.	4.3
32	58	-56.9	n.o.	-3.9	9.3	29.5	n.d.	3.8
33	56	-57.0	-34	-3.1	9.5	28.5	n.d.	4.1
34	55	-57.3	n.o.	-3.8	8.9	28.4	n.d.	4.3
35	56	-56.6	n.o.	-3.3	9.1	29.5	n.d.	3.9
36	53	-57.1	n.o.	-3.1	9.2	29.8	n.d.	4.7
37	55	-57.0	n.o.	-3.6	8.9	30.7	n.d.	4.0
38	53	-57.2	n.o.	-3.4	9.3	30.0	n.d.	5.0
39	55	-57.0	n.o.	-3.5	9.3	29.1	n.d.	4.1
40	56	-57.2	n.o.	-3.9	8.7	28.6	n.d.	3.8
41	54	-56.9	n.o.	-3.8	8.8	29.1	n.d.	4.1
42	54	-57.3	-28	-4.0	9.1	27.1	n.d.	4.4
43	58	-57.1	n.o.	-3.4	8.8	28.9	n.d.	4.9
44	60	-57.2	n.o.	-3.4	8.9	27.9	n.d.	4.2
45	53	-57.3	n.o.	-3.6	9.1	28.5	n.d.	3.3
46	55	-56.9	n.o.	-3.8	8.7	27.9	n.d.	4.7
47	55	-57.1	n.o.	-3.4	9.0	27.6	n.d.	4.0
48	55	-57.3	n.o.	-3.6	9.1	29.0	n.d.	4.3
49	53	-57.0	n.o.	-3.5	9.1	27.9	n.d.	3.9
50	54	-57.1	n.o.	-3.4	9.1	28.2	n.d.	4.1
51	54	-56.9	n.o.	-3.8	9.2	29.9	n.d.	3.5
52	55	-57.4	n.o.	-3.6	8.9	28.6	n.d.	4.2
53	56	-57.0	n.o.	-3.9	9.0	29.2	n.d.	5.2
54	55	-57.2	n.o.	-3.3	8.9	28.8	n.d.	4.1
55	55	-57.1	n.o.	-3.6	8.9	29.1	n.d.	4.7
56	56	-57.0	n.o.	-4.0	9.5	28.8	n.d.	4.5
57	52	-57.5	n.o.	-3.0	9.1	29.0	n.d.	4.7
58	54	-56.9	-28	-3.7	8.8	29.0	n.d.	3.6
59	57	-57.5	-30	-3.4	8.9	28.4	n.d.	4.1
60	55	-56.8	n.o.	-3.3	9.0	28.2	n.d.	4.7
61	58	-57.0	n.o.	-3.7	8.7	27.1	n.d.	4.4
62	53	-57.2	-30.0	-3.3	8.8	29.2	n.d.	4.4
63	57	-56.9	n.o.	-3.7	8.9	29.4	n.d.	4.4

n.o. = not observed; n.d. = not determined due to abundant decrepitation

Table 6 Fluid inclusion LA-ICP-MS data of magmatic quartz from the RMN area. Values below limit of detection are displayed as <"DL".

Name	Spotsize	Na	K	Li	Rb	Sr	Sn	Cs	W
	µm	wt%	wt%	ppm	ppm	ppm	ppm	ppm	ppm
1	44	5.04	4.24	5650	974	49	112	1343	<18
2	44	5.04	1.13	5051	859	24	52	501	<22
3	60	5.04	8.94	9392	305	46	160	535	12
4	60	5.04	3.69	1090	108	21	574	184	<2
5	60	5.04	5.45	10205	2828	42	1195	6433	14
6	60	5.04	7.79	670	261	26	269	251	<1
7	44	5.04	5.82	3663	2908	<14	2161	4442	<32
8	60	5.04	4.51	5453	940	120	215	1591	<33
9	60	5.04	6.45	925	159	38	1189	255	<6
10	60	5.04	6.78	10893	2079	23	723	467	12
11	60	5.04	8.96	910	173	48	262	300	<12
12	60	5.04	4.41	10836	5099	183	3796	9038	11
13	60	5.04	2.66	11362	867	142	10408	2197	<12
14	60	5.04	2.08	7483	235	14	371	388	7
15	60	5.04	1.28	5078	467	47	348	1726	14
16	60	5.04	1.29	4727	1034	18	443	594	35
17	60	5.04	3.45	11711	1096	67	1791	3254	128
18	60	5.04	6.65	2307	700	143	1639	390	10
19	60	5.04	9.14	2981	628	145	2652	1089	<5
20	60	5.04	5.55	8917	2577	26	16359	5949	53
21	60	5.04	1.83	8032	1230	17	20966	2663	22
22	60	5.04	4.99	5850	1156	23	419	2192	38
23	60	5.04	5.37	1305	373	65	26414	1274	9
24	60	5.04	7.45	9501	2733	21	7958	6230	64
25	60	5.04	2.74	11823	2634	15	971	4610	42
26	60	5.04	9.40	531	204	164	2002	242	21
27	60	5.04	5.59	7211	445	<12	1298	1689	<31
28	60	5.04	8.83	345	177	144	699	166	7
29	60	5.04	1.20	192	14	29	15880	12	<2
30	60	5.04	1.05	<115	40	54	26247	136	<6

31	60	5.04	2.08	1116	150	22	144	285	2
32	60	5.04	6.42	795	321	521	761	753	<5
33	60	5.04	2.86	6974	902	49	783	3233	2
34	60	5.04	5.53	5348	372	81	190	757	15
35	60	5.04	2.20	12341	1288	6	337	10545	14
36	60	5.04	2.87	11741	927	57	777	3104	7
37	60	5.04	5.75	42	9	16	1177	11	<3
38	60	5.04	3.76	11792	5047	5	239	9465	23
39	60	5.04	1.10	12461	1683	8	118	9864	15
40	60	5.04	2.64	11733	4277	18	254	10370	19
41	60	5.04	2.75	11356	1761	8	68	8081	10
42	60	5.04	2.74	11834	2210	6	256	8741	8
43	60	5.04	2.93	12248	4715	17	235	13871	<2

Table 7 Fluid inclusion LA-ICP-MS data of metamorphic quartz from the Kibuye area. Values below limit of detection are displayed as <"DL".

Name	Spotsize	Na	K	Li	Rb	Sr	Sn	Cs	W
	µm	wt%	wt%	ppm	ppm	ppm	ppm	ppm	ppm
1	44	1.69	1.20	<270	<22	26	47	<12	24
2	60	1.69	0.17	53	5	384	81	<2	2
3	60	1.69	0.34	<293	<29	115	41	12	<14
4	60	1.69	2.41	<2005	<168	2977	292	<87	<89
5	60	1.69	0.71	<851	<76	80	254	59	64
6	60	1.69	0.20	<13	12	485	8	11	1
7	60	1.69	0.13	<289	<26	295	600	<11	<13
8	60	1.69	0.25	<99	10	44	9	<4	5
9	60	1.69	0.81	<227	22	124	81	<10	10
10	60	1.69	0.54	<33	9	482	71	1	<1
11	60	1.69	0.12	<114	<9	148	15	<4	5
12	60	1.69	0.17	94	<7	10	47	5	3
13	60	1.69	0.45	<328	<26	71	131	<13	15
14	60	1.69	0.39	<305	<24	29	129	<14	<14
15	60	1.69	1.72	<276	<27	62	669	8	<15
16	60	1.69	0.43	<60	5	7	6215	<2	<3
17	60	1.69	1.97	<286	<27	208	629	11	<16
18	60	1.69	0.05	<101	<8	5	134	<4	<4
19	60	1.69	1.06	<113	9	28	249	<5	<6
20	60	1.69	0.60	<195	19	302	186	<10	<12

21	60	1.69	0.03	<44	<3	2	<2	<2	2
22	60	1.69	0.91	18	8	26	19	1	3
23	60	1.69	2.89	<78	56	114	140	30	5
24	60	1.69	1.35	<176	83	300	292	<8	8
25	60	1.69	0.39	162	10	40	33	<3	12
26	60	1.69	0.20	177	<9	18	38	<4	<4
27	60	1.69	0.23	<87	<8	18	306	7	<4
28	60	1.69	0.15	112	<7	8	24	<3	23
29	60	1.69	1.81	<94	26	202	189	4	<5
30	60	1.69	0.16	167	<14	462	99	24	<8
31	60	1.69	0.14	91	<6	5	126	8	<3
32	60	1.69	0.77	63	95	20	42	1	2
33	60	1.69	2.18	51	13	12	488	2	3
34	60	1.69	3.69	64	34	21	30	1	1
35	60	1.69	0.34	<191	<18	14	13	<8	<9
36	60	1.69	2.35	72	15	35	29	<4	<5
37	60	1.69	1.36	155	28	25	67	6	4
38	60	1.69	5.36	<24	14	7	2	<1	<1
39	60	1.69	0.38	164	28	30	51	<4	<4
40	60	1.69	0.96	<103	26	26	24	6	<5
41	60	1.69	0.45	280	<20	20	95	15	<12

Table 8 Geochemistry of the magmatic and metamorphic fluid endmembers. Values are in ppm.

	Rb	Cs	Sn
Magmatic fluid (RMN area, n = 43, median)	885	1640	769
Metamorphic fluid (Kibuye area, n = 41, median)	14	6	81

Table 9 Calculations of the fluid-crystal coefficients for Rb, Sn and Cs in muscovite (using the datasets of Adam and Green, 2006; Hu et al., 2008; Icenhower and London, 1995; Zajacz et al., 2008)

	$K_{d,muscovite}$				K_{fm}				$K_{cf,muscovite}$
	range	reference*	used value		range	condition	reference *	used value	
Rb	0.96 - 1.75	[1]	1.51		0.16 - 1.08		[3]	0.54 (mean)	2.8

Cs	0.16 - 0.36	[1]	0.24		1.4 - 8.6	fluid compatible	[3]	1.4 and 8.6		0.17 and 0.03
Sn	0.05 - 0.28	[2]	0.05		0.00129 - 0.137	(ASI > 1)	[4]	0.05 (mean)		1

* [1] = Icenhower & London, 1995; [2] = Adam & Green, 2006; [3] = Zajacz et al., 2012; [4] = Hu et al, 2008

	03J	19J	23J	44J	47J	49J	52J	53J	62J	67J	08N
	P	P	P	P	P	P	P	P	P	P	P
Al_2O_3	34.89	33.77	33.61	37.64	37.63	36.10	36.87	36.30	34.13	36.77	37.24
FeO	2.25	2.52	3.77	0.53	0.53	1.06	0.93	1.27	3.30	0.70	0.98
K_2O	10.05	9.59	10.01	10.35	10.47	10.16	10.14	10.02	10.23	9.89	9.53
MgO	0.02	0.12	0.11	0.02	0.02	0.04	<0.01	<0.01	0.37	0.06	0.02
MnO	0.08	0.04	0.14	0.03	0.03	0.15	0.06	0.07	0.09	0.05	0.02
Na_2O	0.47	0.57	0.44	0.57	0.56	0.49	0.58	0.66	0.51	0.77	0.89
SiO_2	43.93	43.33	44.01	44.82	44.80	44.66	44.40	44.50	44.93	44.04	44.95
TiO_2	0.02	0.03	0.05	0.06	0.07	0.04	0.02	0.02	0.22	0.03	0.02
ZnO	0.054	0.034	0.067	0.023	0.024	0.111	0.048	0.069	0.048	0.008	0.016
Li	0.092	0.117	0.199	0.012	0.011	0.058	0.039	0.045	0.184	/	0.017
Ba	0.002	0.003	0.004	0.006	0.008	0.002	0.001	0.001	0.010	0.016	0.002
Rb	0.305	0.169	0.237	0.248	0.270	0.503	0.446	0.404	0.177	0.197	0.534
H_2O*	4.34	4.25	4.32	4.49	4.49	4.44	4.45	4.43	4.40	4.40	4.51
Sum oxides	96.11	94.25	96.52	98.53	98.62	97.25	97.50	97.34	98.23	96.72	98.17

	17N	35N	37N	39N	50N	51N	54N	57N	17J	58J	59J
	P	P	P	P	P	P	P	P	Q	Q	Q
Al_2O_3	36.63	36.65	36.97	36.85	37.94	36.70	37.47	37.58	34.67	34.09	35.41
FeO	1.24	1.23	0.78	0.56	0.35	0.77	0.42	0.46	2.35	1.08	1.96
K_2O	9.97	8.79	9.93	9.18	10.19	9.68	9.79	9.63	9.82	9.08	9.51
MgO	0.07	0.10	0.02	0.09	0.01	0.09	0.01	0.01	0.16	0.07	0.23
MnO	0.03	0.04	0.07	0.06	0.09	0.07	0.07	0.04	0.03	0.02	0.02
Na_2O	0.71	0.58	0.50	0.43	0.56	0.59	0.69	0.68	0.59	0.79	0.66

SiO_2	44.79	45.22	44.97	44.80	45.02	44.73	44.42	44.28	44.57	45.16	45.59
TiO_2	0.10	0.11	0.11	0.06	0.08	0.11	0.05	0.01	0.02	0.34	0.51
ZnO	0.016	0.020	0.037	0.031	0.029	0.028	0.023	0.016	0.019	0.005	0.005
Li	0.057	0.056	0.046	0.078	0.044	0.043	0.039	0.029	0.114	0.046	/
Ba	0.030	0.018	0.008	0.009	0.005	0.017	0.002	0.002	0.013	0.225	0.075
Rb	0.146	0.262	0.406	0.396	0.338	0.389	0.365	0.874	0.081	0.048	0.062
H_2O*	4.44	4.46	4.48	4.44	4.51	4.45	4.46	4.51	4.35	4.36	4.46
Sum oxides	98.00	97.20	97.86	96.50	98.78	97.22	97.40	97.22	96.58	95.00	98.35

	69J	07N	21N	32N	45N	52aN	52bN	58N	62N	64N	66N
	Q	Q	Q	Q	Q	Q	Q	Q	Q	Q	Q
Al_2O_3	34.46	37.06	35.37	34.76	34.30	37.52	34.00	35.17	34.44	35.18	36.58
FeO	3.12	0.87	2.10	1.71	2.74	0.43	2.54	1.87	1.92	2.22	1.31
K_2O	10.14	8.62	10.08	9.96	9.83	9.81	9.68	9.98	9.36	10.03	8.60
MgO	0.22	0.06	0.28	0.48	0.49	0.01	0.41	0.32	0.40	0.42	0.07
MnO	0.08	0.01	0.05	0.02	0.02	0.07	0.04	0.03	0.02	0.02	0.01
Na_2O	0.54	1.23	0.69	0.64	0.60	0.69	0.64	0.64	0.75	0.65	1.13
SiO_2	45.14	45.45	45.61	46.38	45.48	44.51	44.58	44.96	45.98	45.54	45.98
TiO_2	0.12	0.43	0.25	0.32	0.34	0.06	0.40	0.13	0.53	0.59	0.18
ZnO	0.048	0.005	0.015	0.006	0.023	0.024	0.018	0.005	0.010	0.011	0.005
Li	0.167	0.012	0.086	0.104	/	/	0.152	0.043	0.065	0.084	/
Ba	0.005	0.155	0.064	0.053	0.053	0.002	0.057	0.035	0.243	/	0.023
Rb	0.165	0.075	0.173	0.053	0.175	0.378	0.150	0.059	0.236	0.238	0.061
H_2O*	4.41	4.49	4.47	4.47	4.43	4.47	4.36	4.40	4.45	4.48	4.49
Sum oxides	98.28	98.23	98.91	98.75	98.25	97.59	96.66	97.51	97.86	99.14	98.36

P = pegmatitic muscovite, Q = quartz vein muscovite, / = not analyzed

*H_2O calculated stoechiometrically according to Tindle & Webb (1990)

Highlights

- Peribatholitic Sn-quartz veins often show secondary overprinting signatures.
- Fluid mixing was quantified by muscovite and fluid inclusion geochemistry
- Fluid mixing plays an important role in the genesis of Sn-quartz veins.

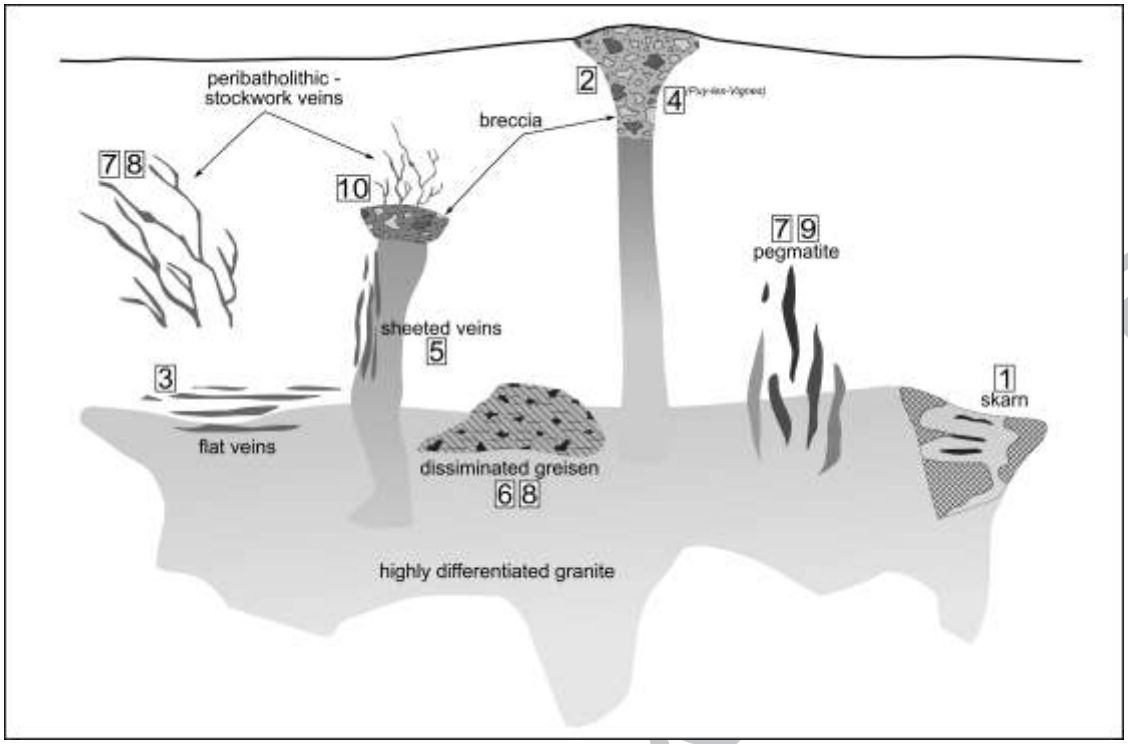

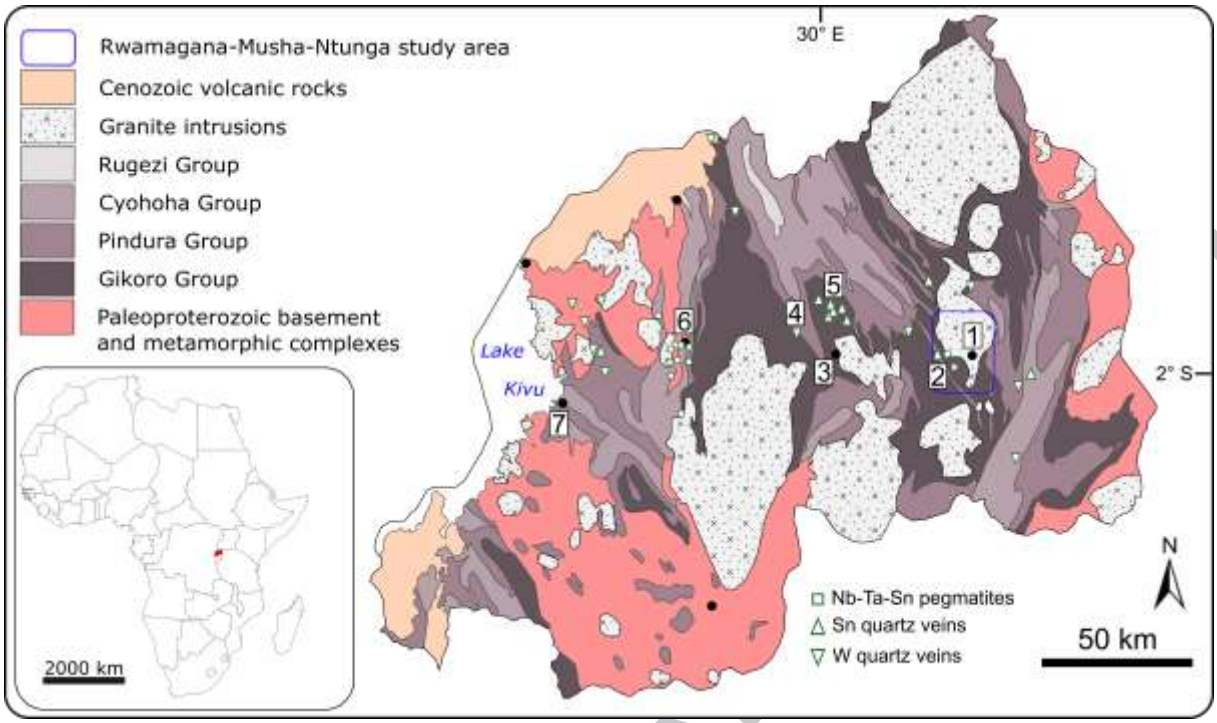

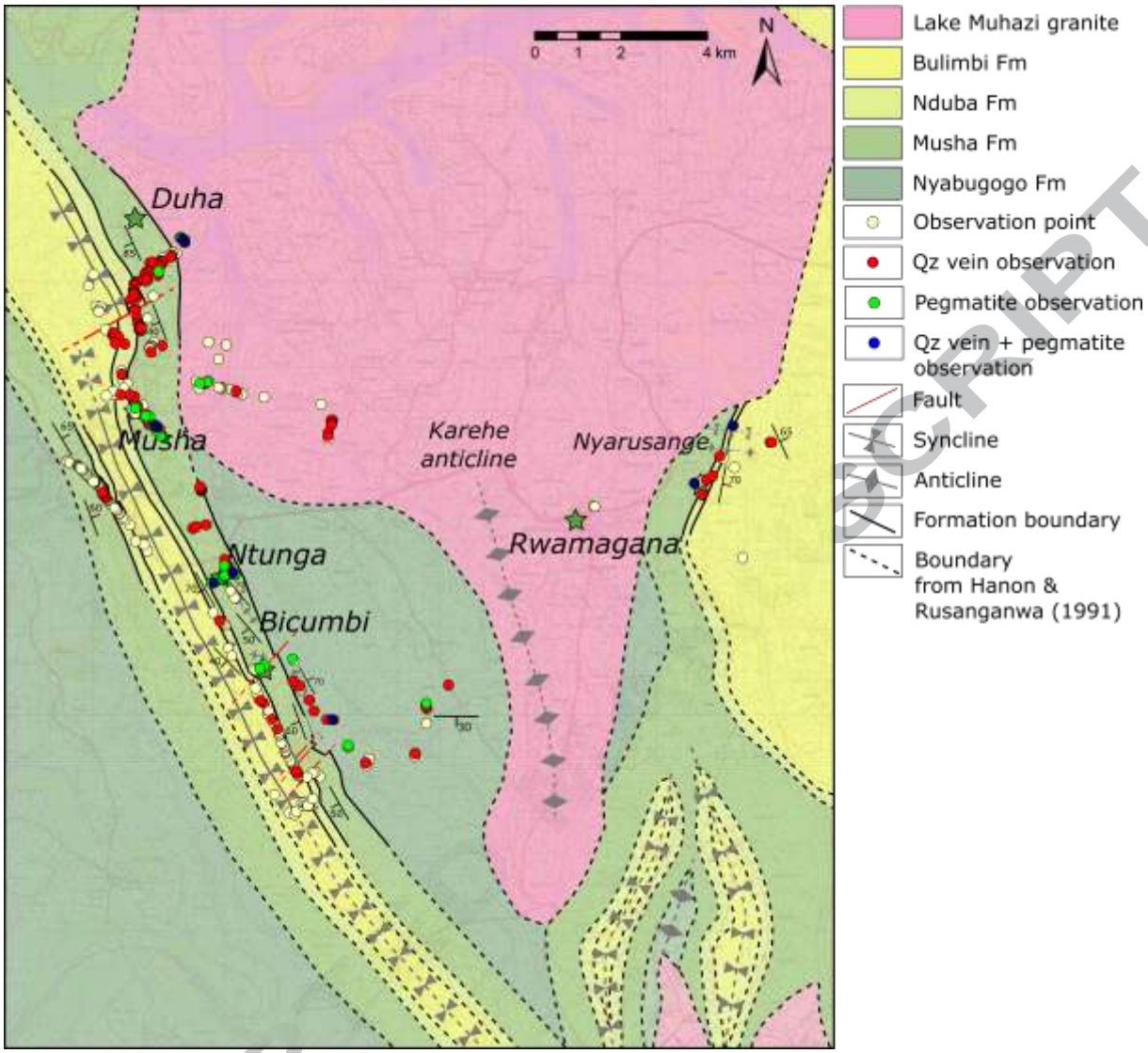

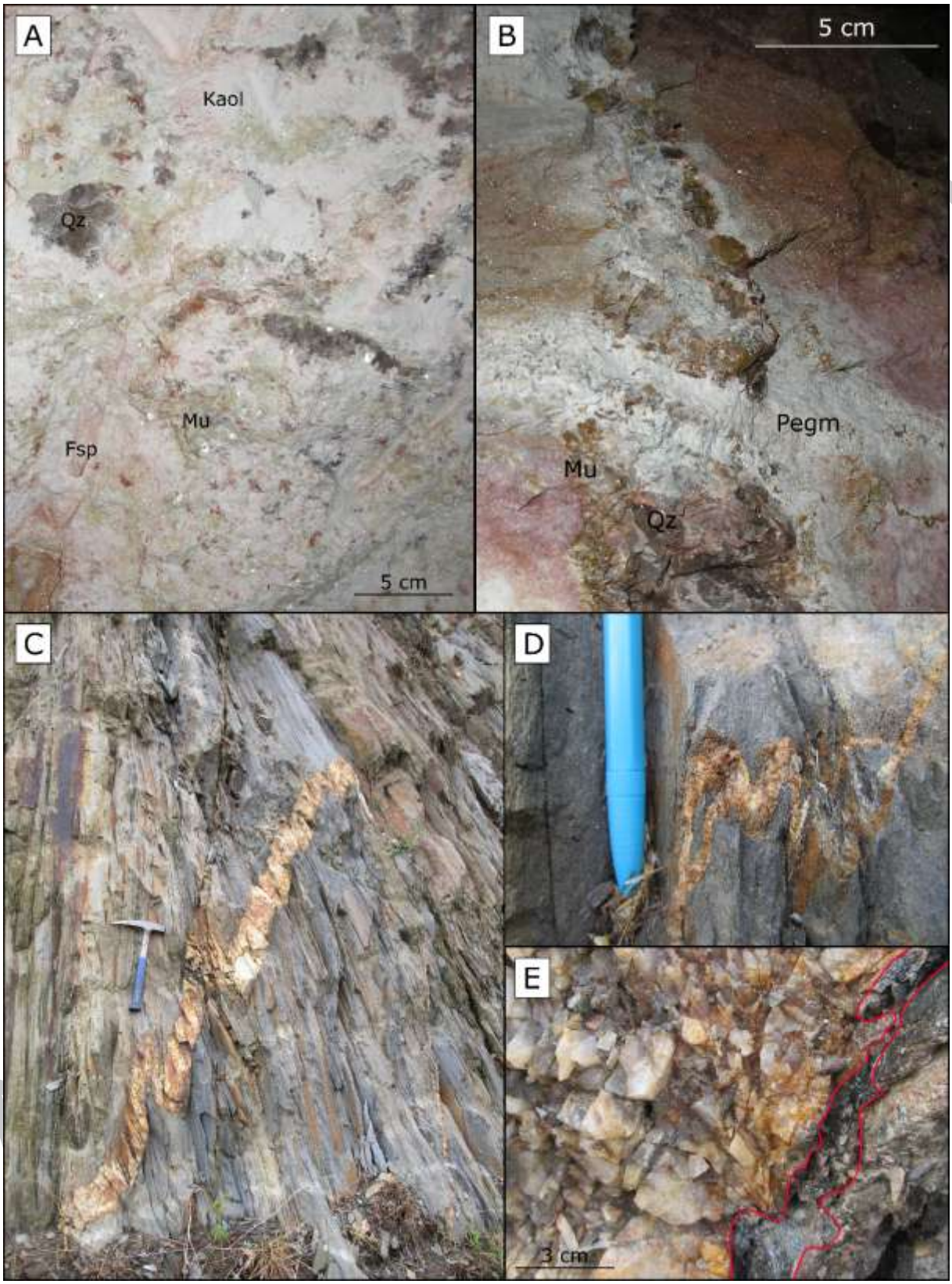
A
Kaol
Qz
Mu
Fsp
5 cm
B
5 cm
Pegm
Mu
Qz
C
D
E
3 cm

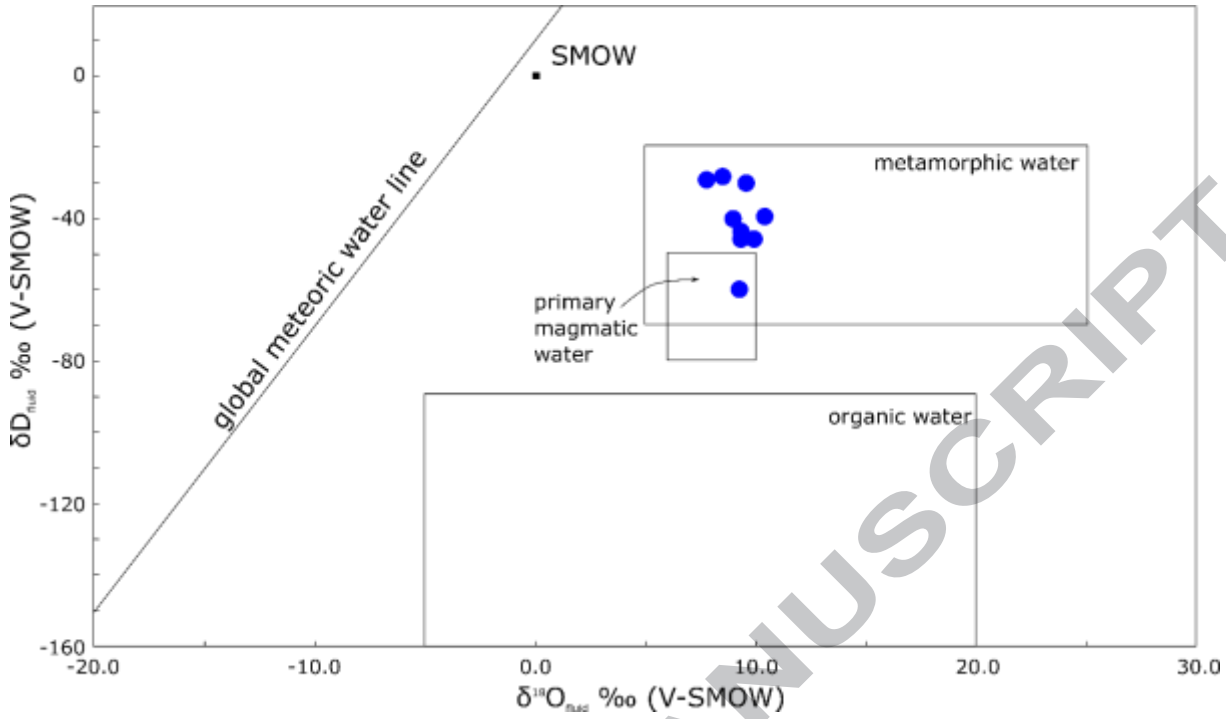

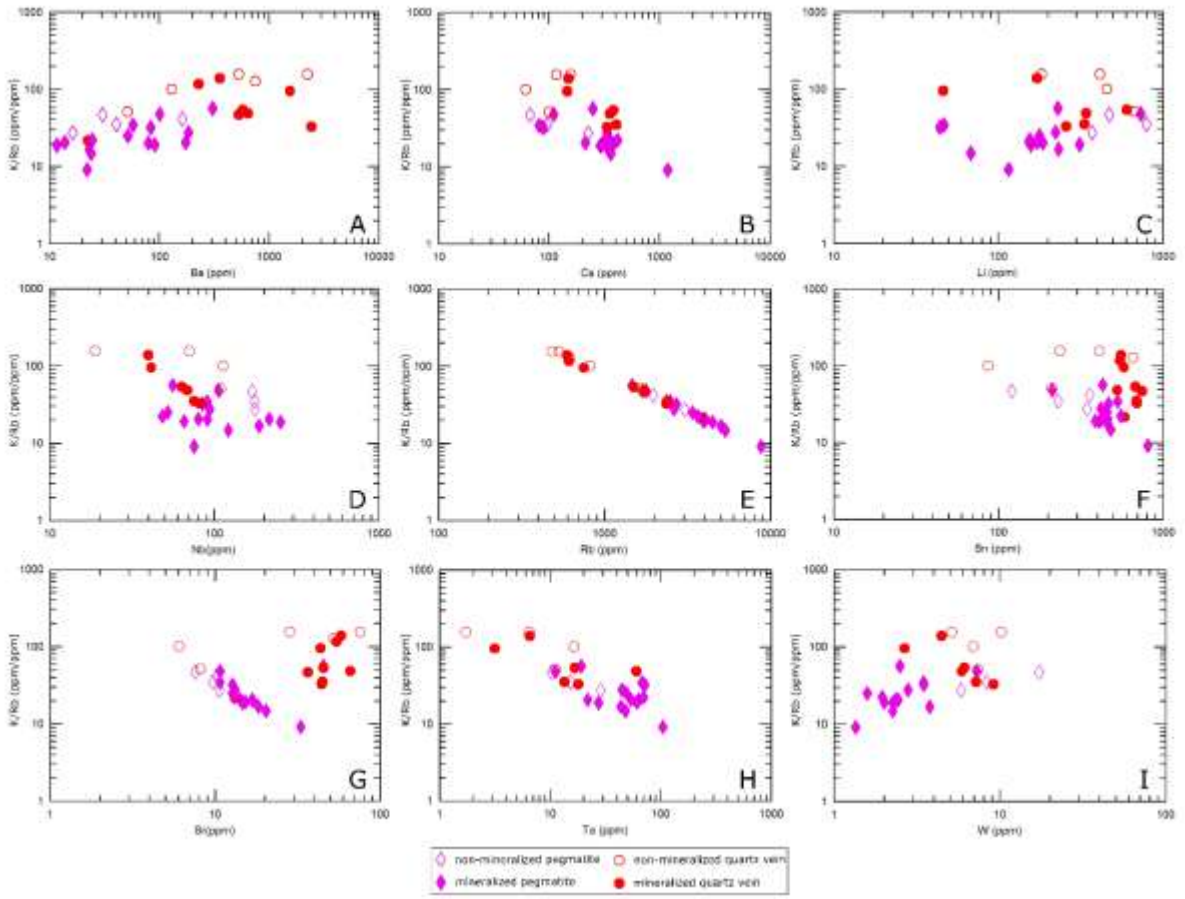

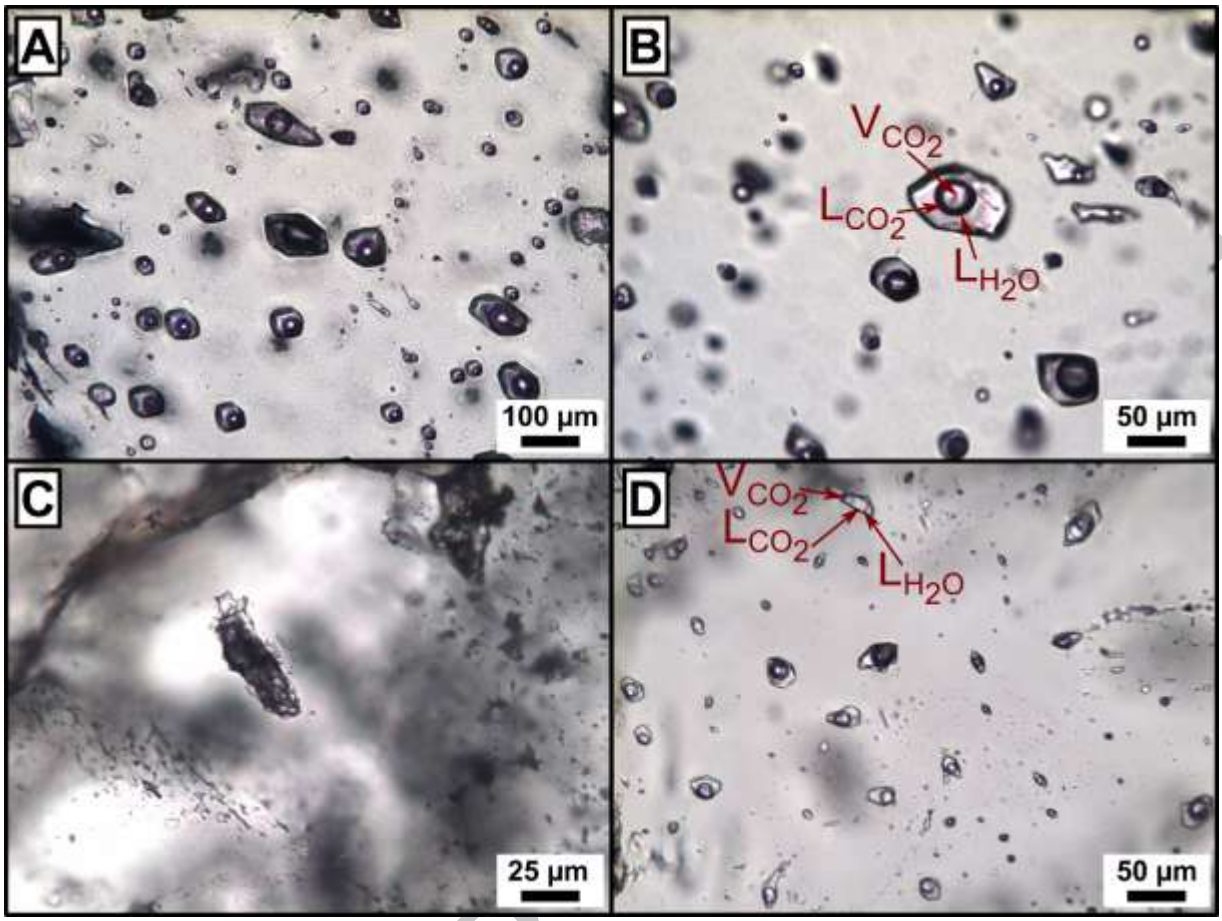

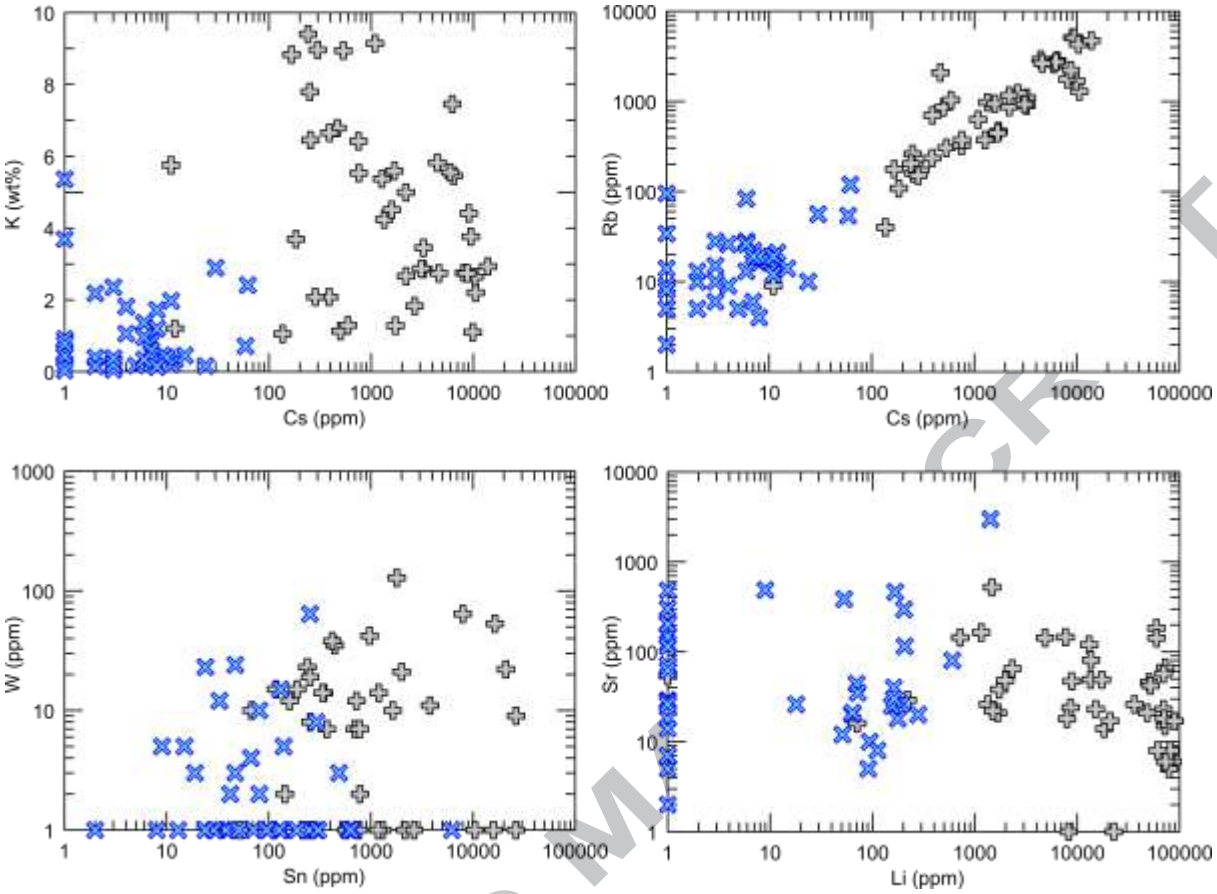

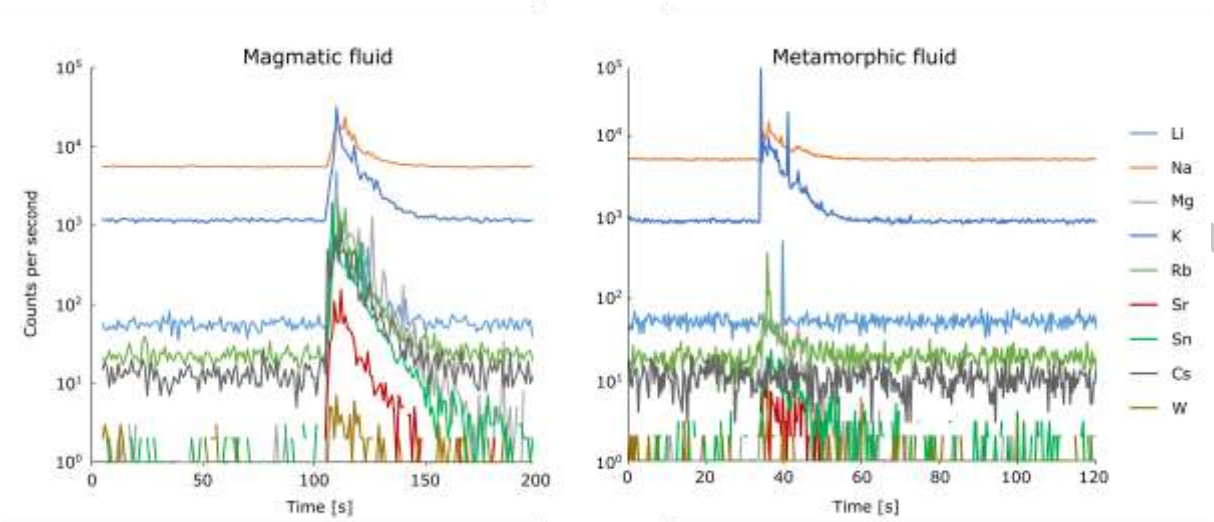

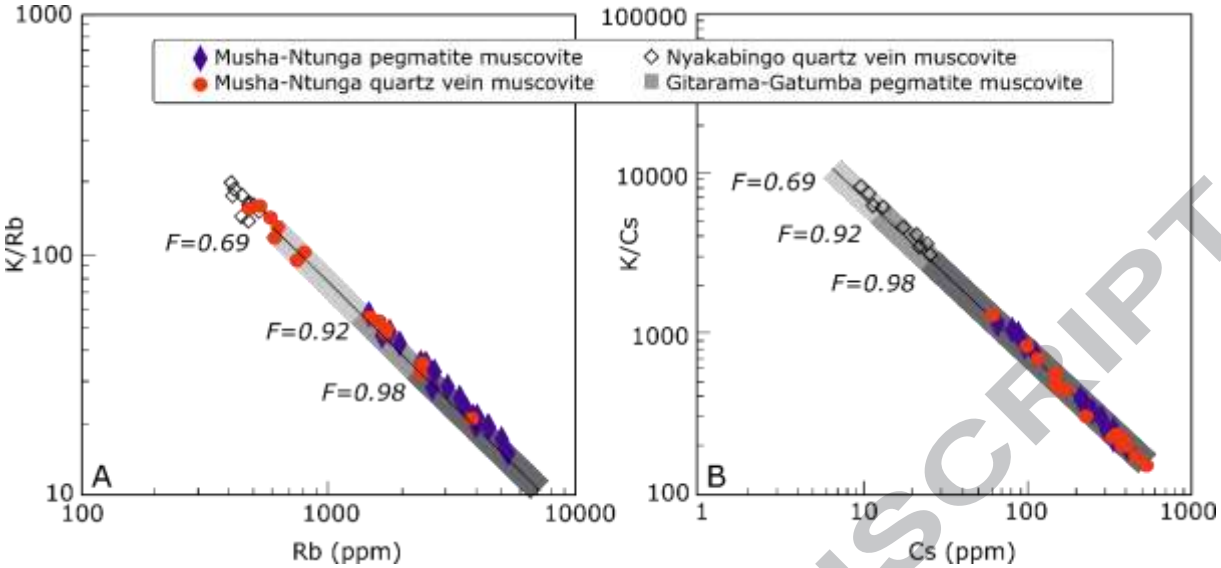

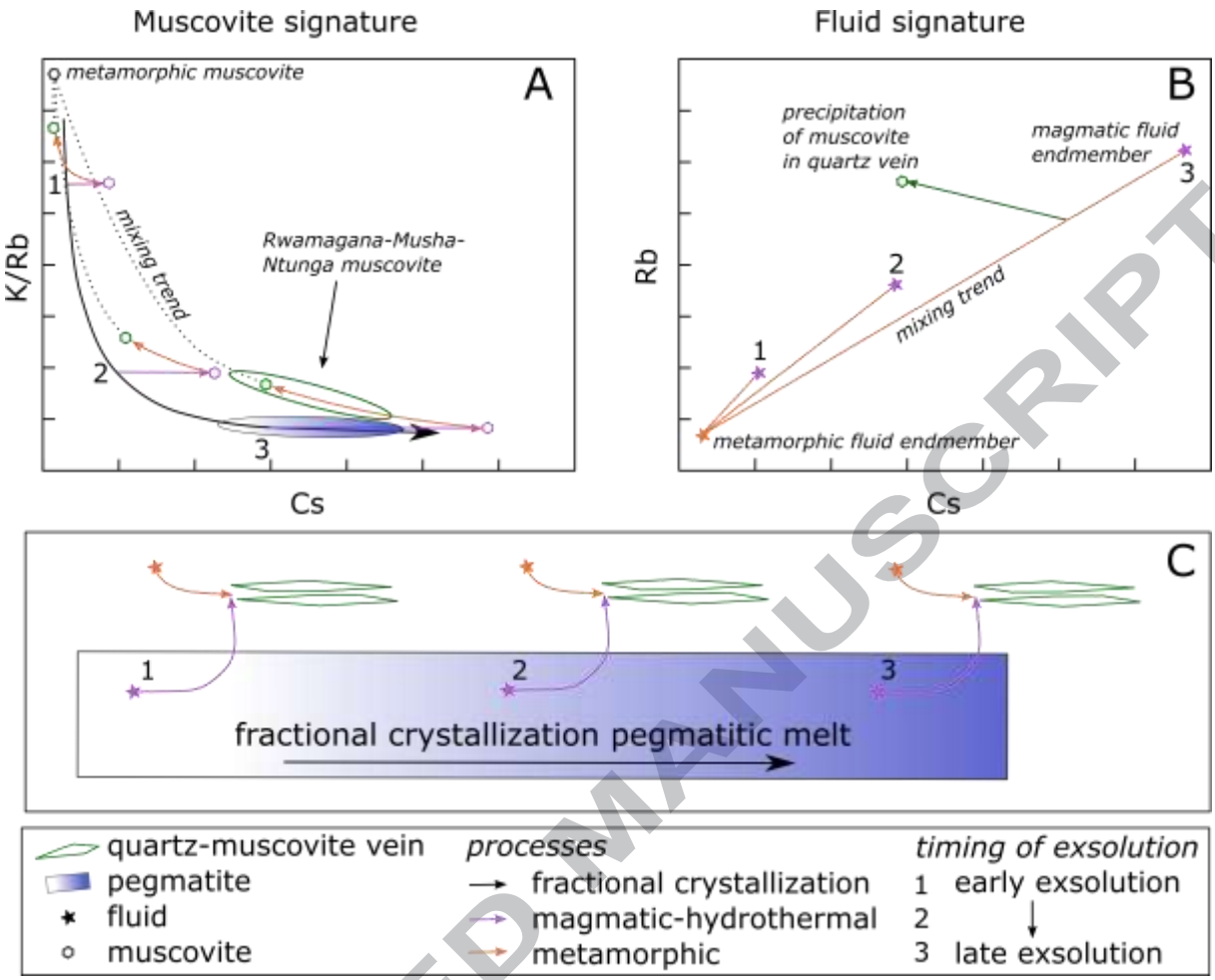

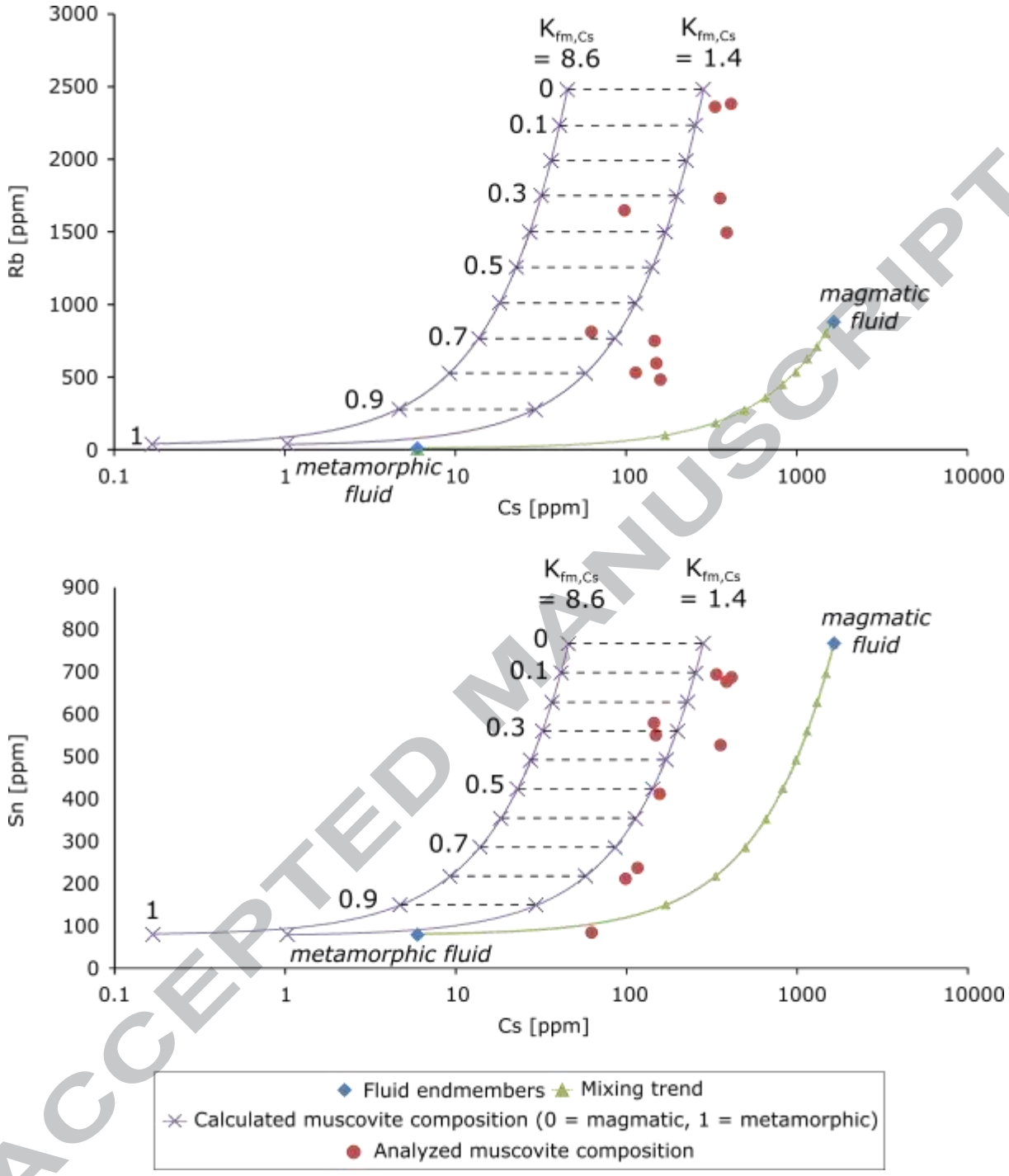

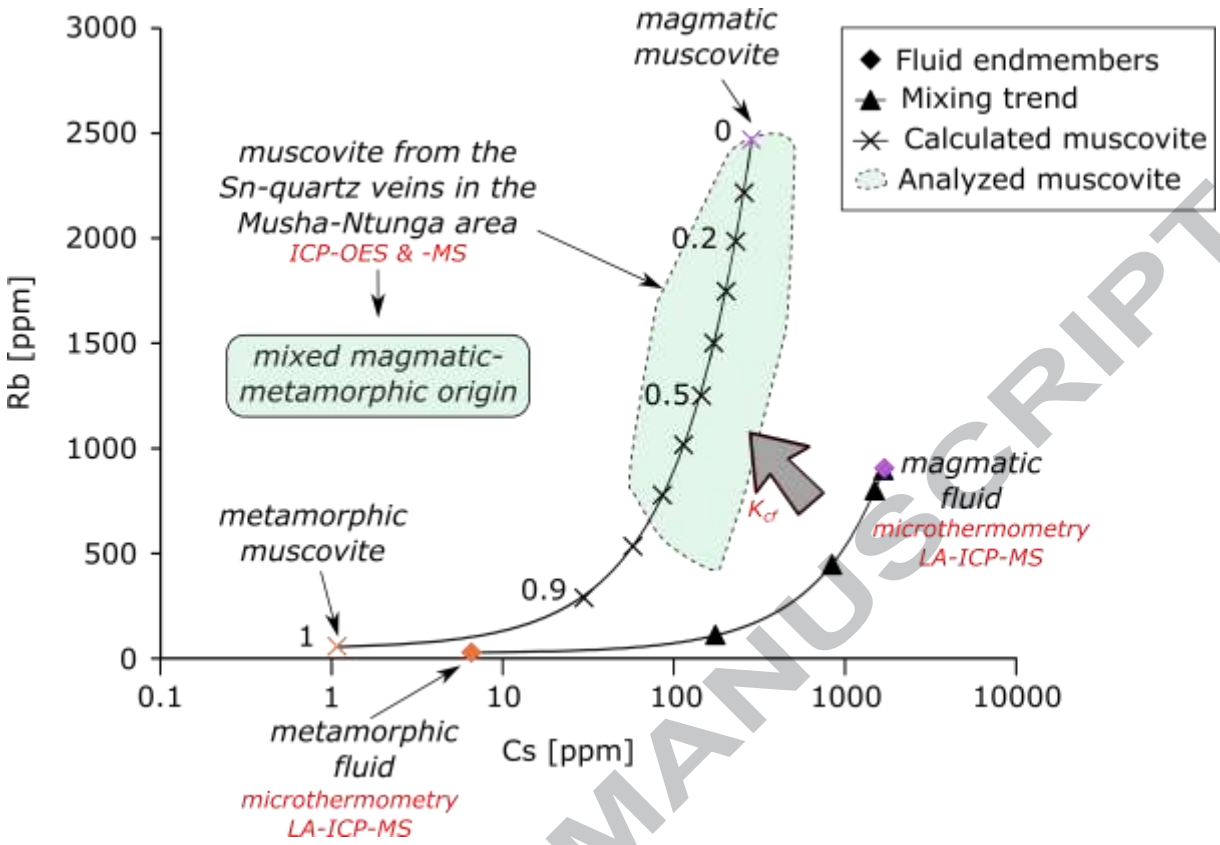

Graphical abstract